

₁ Low p_T dielectron production in Au+Au collisions at
₂ $\sqrt{s_{NN}} = 200$ GeV and U+U collisions at $\sqrt{s_{NN}} = 193$
₃ GeV at STAR

₄ Shuai Yang
₅ syang@rcf.rhic.bnl.gov

₅ January 4, 2018

6 Contents

7 1 Data Set and Event Selection	3
8 2 Electron Identification	5
9 2.1 Track Selection	5
10 2.2 Electron Identification Cuts	5
11 2.3 Electron Purity	7
12 3 Pair Reconstruction and Background Subtraction	11
13 3.1 Like-sign Technique	14
14 3.2 Mixed-Event Technique	15
15 3.3 Photon Conversion Removal	17
16 3.4 Raw Signals	20
17 4 Efficiency and Acceptance Corrections	28
18 4.1 Single Track Efficiency	28
19 4.1.1 TPC Tracking Efficiency	29
20 4.1.2 nHitsDedx Cut Efficiency	29
21 4.1.3 TOF Matching Efficiency	30
22 4.1.4 eID Cuts Efficiency	31
23 4.2 Pair Efficiency	33
24 5 Hadronic Cocktail Simulation	38
25 6 Systematic Uncertainties	46
26 7 Physics Results	49
27 7.1 Consistency Check Between Run10 and Run11 Au + Au Collisions	49
28 7.2 Low p_T e^+e^- Paper Plots	49
29 7.3 The model calculation of photon-photon interaction in peripheral Au + Au collisions (done by Wangmei Zha)	57

31 1 Data Set and Event Selection

32 The data sets used in this analysis are from Au + Au collisions at $\sqrt{s_{NN}} = 200$ GeV
 33 during the 2010 (Run10) and 2011 (Run11) RHIC runs, U + U collisions at $\sqrt{s_{NN}} = 193$
 34 GeV in 2012 (Run12). The minimum-bias (MB) trigger is defined as a coincidence between
 35 the two VPDs, a coincidence between the two ZDCs, and an online collision vertex cut.
 36 Moreover, a pile-up protection at the trigger level was applied for the data taking.

37 Events used in this analysis are required to have a valid collision vertex (primary vertex)
 38 within 30 cm of the TPC center along z direction (the direction along beam axis) to ensure
 39 uniform a TPC acceptance. Furthermore, the distance between the collision vertex along z
 40 direction constructed by the TPC (V_z^{TPC}) and the VPD (V_z^{VPD} , fast detector) is within 3
 41 cm to reject the event with wrong reconstructed TPC vertex from different bunch-crossing
 42 collisions. To reject the events from the beam hitting the beam pipe, vertex with a radial
 43 length less than 2 cm with respect to the beam pipe center is required. After event selection,
 44 A total of ~ 720 million Au + Au and ~ 270 million U + U minimum-bias events are finally
 45 used in this analysis. Table 1 lists the event selection criteria.

Table 1: Event selection in Au + Au collisions at 200 GeV and U + U collisions at 193 GeV.

Event Selection Criteria
$ V_r < 2$ cm
$ V_z^{TPC} < 30$ cm
$ V_z^{TPC} - V_z^{VPD} < 3$ cm

46 The centrality in Au + Au or U + U collisions is defined using the uncorrected charged
 47 particle density (dN_{ch}/dy). The primary tracks with $|\eta| \leq 0.5$, $dca \leq 3$ cm and $nHitsFit \geq$
 48 10 (number of hits used for track fitting) are used to calculate the dN_{ch}/dy . Furthermore, the
 49 dN_{ch}/dy is corrected for the V_z^{TPC} and luminosity dependence to account for the acceptance
 50 and efficiency changes on the measured dN_{ch}/dy . Then the dN_{ch}/dy is compared to a Monte
 51 Carlo (MC) Glauber calculation [1] to delineate the centrality bins, the equivalent number
 52 of binary nucleon + nucleon collisions (N_{bin} or N_{coll}) and the number of participants (N_{part})
 53 for nucleus + nucleus collisions. Table 2 and Table 3 list the $\langle N_{coll} \rangle$, $\langle N_{part} \rangle$ from Glauber
 54 model for each defined centrality bin in Au + Au collisions at $\sqrt{s_{NN}} = 200$ GeV, U + U
 55 collisions at $\sqrt{s_{NN}} = 193$ GeV, respectively. The 0-80% and finer centrality-bins within this
 56 range are used in this analysis, because the 80-100% centrality has significant trigger bias
 57 due to vertex inefficiency at low charged particle density.

Table 2: Centrality bins and corresponding $\langle N_{coll} \rangle$, $\langle N_{part} \rangle$ in Au + Au at 200 GeV.

Centrality	$\langle N_{coll} \rangle$	$\langle N_{part} \rangle$	Centrality	$\langle N_{coll} \rangle$	$\langle N_{part} \rangle$
0-5%	1048.11	349.64	5-10%	838.41	302.23
10-15%	663.04	256.76	15-20%	524.31	217.77
20-25%	411.86	183.75	25-30%	320.78	154.24
30-35%	246.95	128.30	35-40%	186.69	105.44
40-45%	138.71	85.48	45-50%	101.51	68.32
50-55%	72.79	53.86	55-60%	51.62	41.74
60-65%	35.64	31.62	65-70%	23.96	23.35
70-75%	15.98	16.96	75-80%	10.54	12.11

Table 3: Centrality bins and corresponding $\langle N_{coll} \rangle$, $\langle N_{part} \rangle$ in U + U at 193 GeV.

Centrality	$\langle N_{coll} \rangle$	$\langle N_{part} \rangle$	Centrality	$\langle N_{coll} \rangle$	$\langle N_{part} \rangle$
0-5%	1281.26	414.87	5-10%	1010.97	355.42
10-15%	798.53	300.92	15-20%	628.01	253.66
20-25%	490.60	212.84	25-30%	379.86	177.48
30-35%	290.31	146.78	35-40%	217.35	119.63
40-45%	160.03	96.34	45-50%	115.69	76.43
50-55%	81.76	59.55	55-60%	56.98	45.73
60-65%	38.36	34.01	65-70%	25.06	24.55
70-75%	16.28	17.46	75-80%	10.23	11.98

58 2 Electron Identification

59 The same electron identification technique is employed in both
 60 **Au + Au collisions at 200 GeV and U + U collisions at 193 GeV.**
 61 The detailed electron selection criteria in Au + Au collisions at
 62 **200 GeV can be found in p3-p6 of [https://drupal.star.bnl.gov/](https://drupal.star.bnl.gov/STAR/system/files/NOTEv9_0.pdf)**
 63 **STAR/system/files/NOTEv9_0.pdf**. The following three sub-sections
 64 **are for U + U collisions at 193 GeV.**

65 2.1 Track Selection

66 The interested electrons (including positrons if not specified) are mainly
 67 from the collision point or short-lived particle decays close to the collision
 68 point. Thus the primary tracks, including the primary vertex for the track
 69 fitting resulting in a better momentum resolution, are used in this analysis.
 70 The primary tracks are required to satisfy the following selection criteria:
 71 p_T is ≥ 0.2 GeV/ c to ensure that the track can pass through the TPC;
 72 the Distance of Closest Approach (dca) to the primary vertex is ≤ 1 cm
 73 to reduce contributions from secondary decays; the number of hit points
 74 (nHitsFit) along the track is ≥ 20 (of a maximum of 45) to ensure good
 75 momentum resolution; the ratio of number of hit points along the track over
 76 the number of maximum possible points (nHitsPoss) is ≥ 0.52 to suppress
 77 the possibility of selecting duplicated short tracks from track splitting; the
 78 number of points used for calculating $\langle dE/dx \rangle$ (nHitsDedx) is ≥ 15 to ensure
 79 good dE/dx resolution; at last, the track is required to match with the TOF
 80 and restricted to $|\eta| \leq 1$.

81 2.2 Electron Identification Cuts

82 The electron candidates could be identified by combining the TPC and
 83 TOF. The TPC provides particle identification utilizing the dE/dx , because
 84 different particle species with the same momentum may have different dE/dx .

Table 4: Electron candidates selection criteria in U + U collisions at 193 GeV.

Track Quality Cuts	Electron Identification Cuts
$0.2 \leq p_T \leq 30 \text{ GeV}/c$ $ \eta \leq 1$ $\text{nHitsFit} \geq 20$ $\text{nHitsFit}/\text{nHitsPoss} \geq 0.52$ $\text{nHitsDedx} \geq 15$ $\text{dca} \leq 1 \text{ cm}$	$p < 1 \text{ GeV}/c,$ $1.5625 \times (p - 0.2) - 2 - \mathbf{0.34} \leq n\sigma_e \leq 2 - \mathbf{0.34}$ $p \geq 1 \text{ GeV}/c,$ $-0.75 - \mathbf{0.34} \leq n\sigma_e \leq 2 - \mathbf{0.34}$ $ 1 - 1/\beta \leq 0.025$

85 However, in some momentum regions, the TPC can not identify different
 86 particle species with very similar dE/dx (e.g. e/K at $p \approx 0.5 \text{ GeV}/c$, e/p
 87 at $p \approx 1 \text{ GeV}/c$). Different particle species with the same momentum have
 88 different velocities, thus the TOF with $<80 \text{ ps}$ time resolution can be used
 89 to identify different particle species in the dE/dx crossover regions by precise
 90 velocity information ($1/\beta = ct/l$). The normalized dE/dx , defined in Eq. 1,
 91 instead of dE/dx is used in this analysis. Where $\langle dE/dx \rangle^{\text{Mea.}}$ and $\langle dE/dx \rangle_e^{\text{Th.}}$
 92 represent measured and theoretical dE/dx , and $R_{dE/dx}$ is the STAR TPC
 93 dE/dx resolution (typically $\sim 8\%$).

$$n\sigma_e = \frac{1}{R_{dE/dx}} \log \frac{\langle dE/dx \rangle^{\text{Mea.}}}{\langle dE/dx \rangle_e^{\text{Th.}}} \quad (1)$$

94 By applying the TOF velocity cut, the slow hadrons are rejected from
 95 electrons in the dE/dx overlapping regions, as shown in Fig. 1. After the
 96 TOF velocity cut, the $n\sigma_e$ cut is applied to reject hadrons with almost the
 97 same velocity as electrons, as shown in Fig. 2. The electron sample is then
 98 extracted. A tachyon band is observed in the Fig. 1, that is because TOF hits
 99 from electrons originating from photon conversions in the material between
 100 the TPC and TOF leaving no trace in the TPC are randomly associated
 101 with TPC tracks especially in high-multiplicity collisions [2]. The random
 102 match could also result in some slow hadrons surviving the TOF velocity
 103 cut. Besides the random match, the secondary particles with inaccurate

track length and flight time measurement may also survive the TOF velocity cut. For those survived slow hadrons, if their dE/dx overlap with electrons, there is no way to reject them, as shown in Fig. 2. Thus the electron purity should be estimated, as discussed in Sec. 2.3. For the systematic uncertainty study from hadron contamination, it will be discussed in Sec. 6. Table. 4 lists the track selection criteria and electron identification cuts in U + U collisions at 193 GeV. The $n\sigma_e$ distribution of the pure electron sample is centered at -0.34 instead of 0 due to the imperfect TPC calibration, as shown in Fig. 5. Thus the $n\sigma_e$ cut is shift down 0.34 to account for this effect.

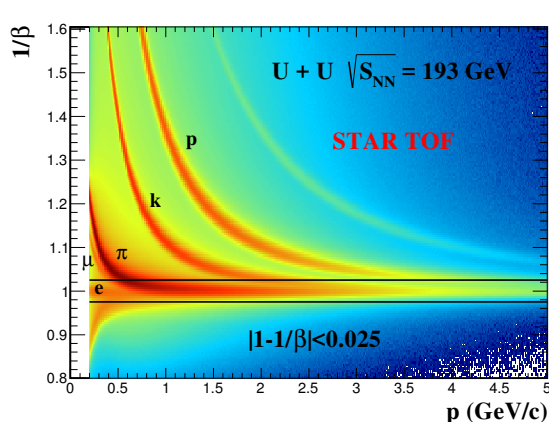


Figure 1: $1/\beta$ vs. particle momentum distribution.

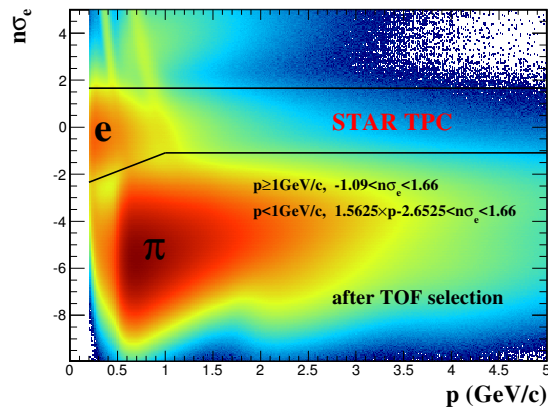


Figure 2: $n\sigma_e$ vs. particle momentum after the high velocity cut applied, as shown in Fig. 1.

2.3 Electron Purity

The pure hadron samples ($\pi/K/p$) are selected by combining tight m^2 and loose $n\sigma_{hadron}$ cuts. The selection criteria and $n\sigma_e$ distribution for each pure hadron sample are shown in Fig. 3. The pure electron sample is from the π^0 Dalitz decay and photon conversion. The invariant mass of the electron pair from photon conversion should be zero. However, the primary track, forced to originate from primary vertex, is used to reconstruct the electron pair invariant mass (see detailed procedure in Sec. 3). That will introduce a artificial

opening angle between electron and positron resulting in a non-zero invariant mass. The angle depends on the distance between the photon conversion point and the primary vertex. Thus the photons converting at different positions result in different invariant mass. The $M_{ee} < 0.015 \text{ GeV}/c^2$ is used to select the π^0 Dalitz decayed and photon conversion electrons with 148:1 (in minimum-bias collisions) signal-to-background ratio, shown in the left panel of Fig. 4. After subtracting the same sign electron pairs from the opposite sign electron pairs, shown in the right panel of Fig. 4, the pure electron sample is thus extracted, shown in Fig. 5. Due to the high charged particle density in U + U collisions at 193 GeV, it is likely to happen that two tracks with same charge and similar momentum are very closed to each other. The two tracks are very likely to be reconstructed into “one track” due to the finite hit position resolution, so called “merged track”. The pion is very abundant in U + U collisions at 193 GeV, thus the “merged π ” should be taken into account for the purity study. The “merged π ” could be selected using the same m^2 cut as normal π but with $n\sigma_\pi > 6$ (“merged π ” is with doubled dE/dx compared to a normal π). The $n\sigma_e$ distribution of each selected pure sample could be fitted by Gaussian function in each fine p_T bin. The mean and sigma of the $n\sigma_e$ distribution as a function of momentum for each pure sample in minimum-bias collisions are shown in Fig. 6 (More fitting details of pure hadron and electron $n\sigma_e$ distributions can be found in <http://www.star.bnl.gov/protected/lfsupc/syang/dielectronPaper/uu193/pureSamples/>). The electron purity is then estimated based on multi-Gaussian fitting to the $n\sigma_e$ distribution after applying TOF velocity cut. The mean and width of each component is constrained by the values in Fig. 6 when multi-Gaussian fitting is performed. Figure 7 shows examples of the multi-Gaussian fitting in three specific momentum regions. In the dE/dx overlap regions (e.g. e/K at $p \approx 0.5 \text{ GeV}/c$, e/p at $p \approx 1 \text{ GeV}/c$), the multi-Gaussian fitting is not reliable. An exponential function is employed to extrapolate the hadron particle yields in the overlapping regions as shown in the left

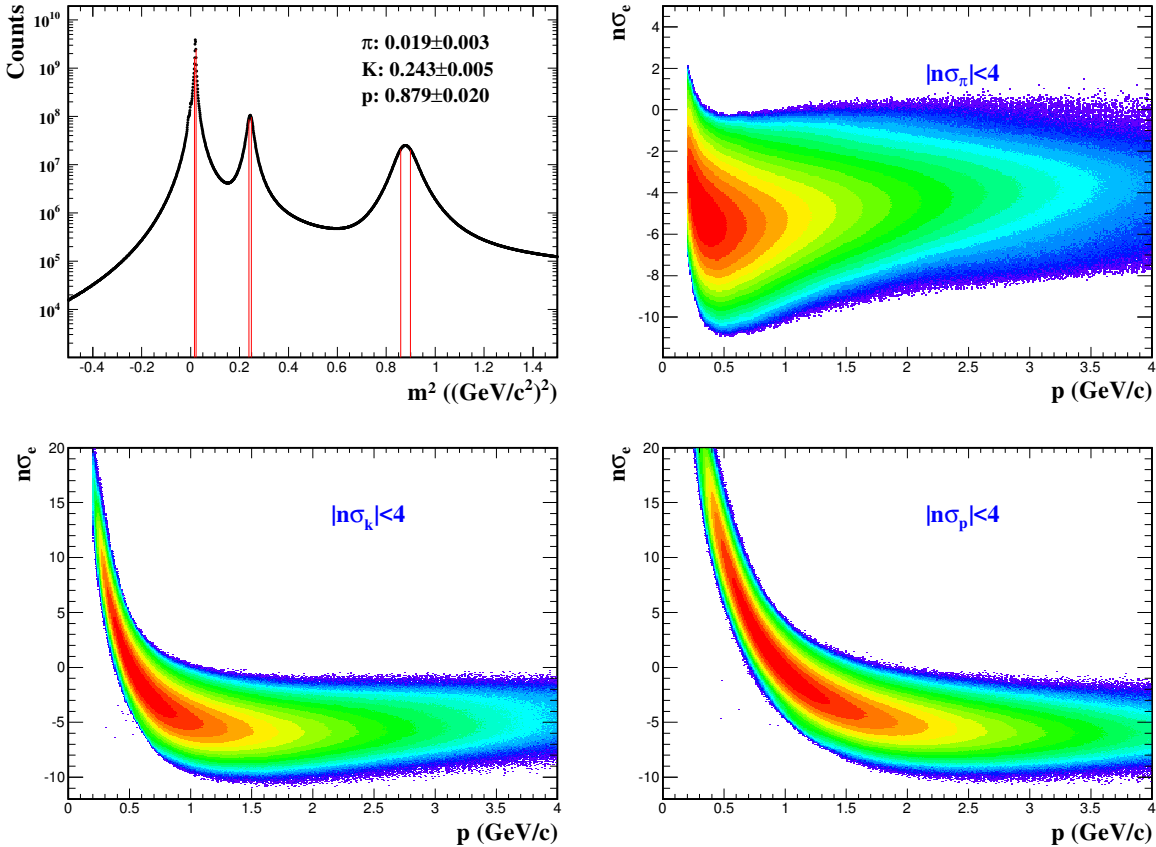


Figure 3: The selection criteria and $n\sigma_e$ distribution as a function of momentum for each pure hadron sample in U + U 193 GeV minimum-bias collisions. (Top Left) m^2 distribution of different particle species and pure hadron m^2 selection criteria. (Top Right) Pure pion sample. (Bottom Left) Pure kaon sample. (Bottom Right) Pure proton sample.

151 panel of Fig. 8. The hadron yields are then constrained, just leaving the
 152 electron yield as a free parameter, in the multi-Gaussian function for re-
 153 fitting. The electron yield from the second-round multi-Gaussian fitting is
 154 extracted to check the fit reliability, shown in the right panel of Fig. 8. The
 155 electron purity difference between these two-round fittings is taken as the
 156 systematic uncertainty. Figure 9 shows the electron purity (overall at $\sim 95\%$)
 157 in U + U minimum-bias collisions at 193 GeV. More details of the multi-
 158 Gaussian fitting can be found in [http://www.star.bnl.gov/protected/
 159 lfsupc/syang/dielectronPaper/uu193/singleTrkEff/nSigmaE/minibias_](http://www.star.bnl.gov/protected/lfsupc/syang/dielectronPaper/uu193/singleTrkEff/nSigmaE/minibias_nSigECutEff.pdf)
 160 [nSigECutEff.pdf](http://www.star.bnl.gov/protected/lfsupc/syang/dielectronPaper/uu193/singleTrkEff/nSigmaE/minibias_nSigECutEff.pdf).

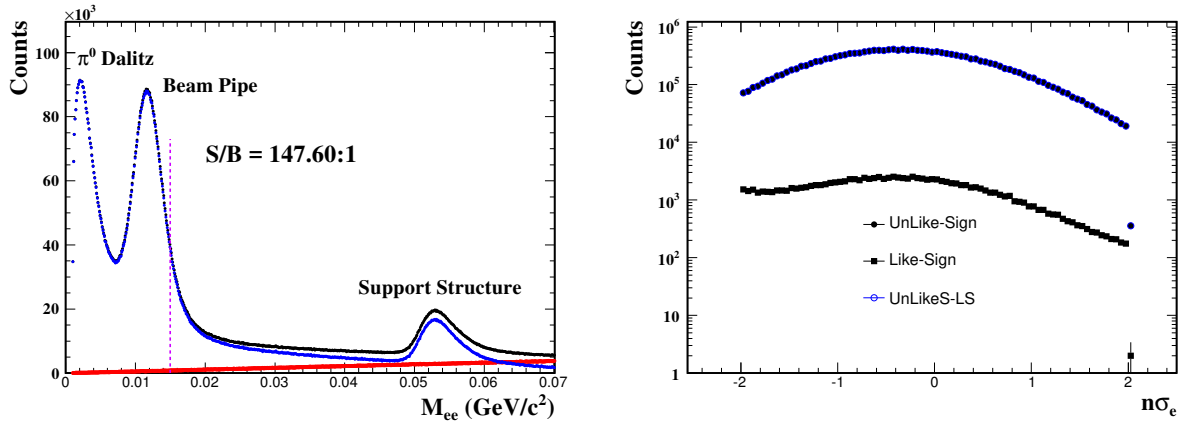


Figure 4: The selection criteria and $n\sigma_e$ distribution of pure electron sample in U + U minimum-bias collisions at 193 GeV. (Left) The invariant mass distribution of π^0 Dalitz decay and photon conversion electron pairs. (Right) The $n\sigma_e$ distribution of π^0 Dalitz decay and photon conversion electrons.

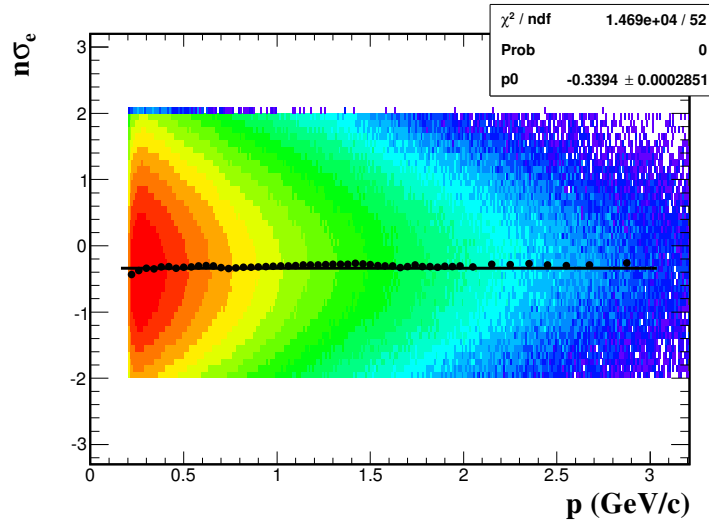


Figure 5: The $n\sigma_e$ distribution of pure electron sample as a function of momentum in U + U minimum-bias collisions at 193 GeV. The mean of the $n\sigma_e$, shown as black dots, is shift to -0.34 due to imperfect TPC dE/dx calibration.

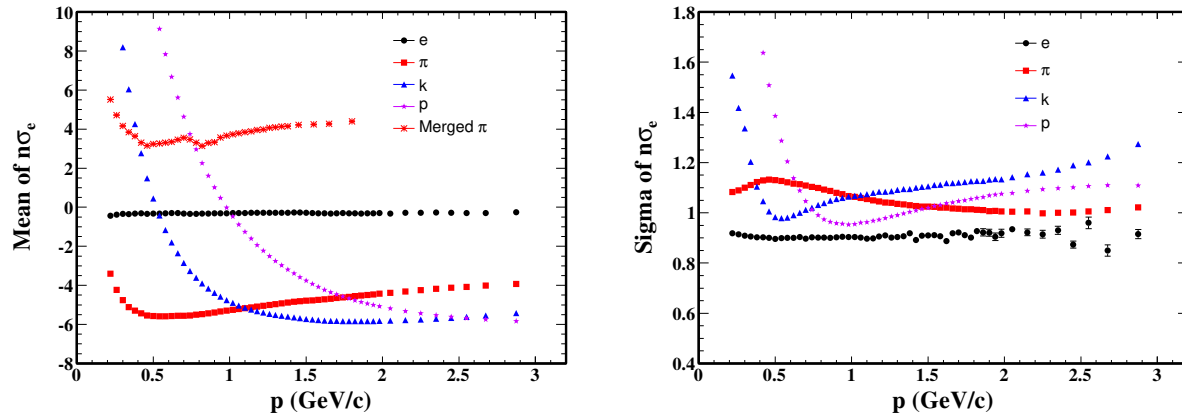


Figure 6: The mean (Left) and sigma (Right) of the $n\sigma_e$ for each pure particle sample as a function of momentum in U + U 193 GeV minimum-bias collisions.

161 3 Pair Reconstruction and Background Subtraction

162 The same technique is employed in both Au + Au collisions
 163 at 200 GeV and U + U collisions at 193 GeV. The detailed fore-
 164 ground and background reconstruction in Au + Au collisions at 200
 165 GeV can be found in p6-p15 of [https://drupal.star.bnl.gov/STAR/
 166 system/files/NOTEv9_0.pdf](https://drupal.star.bnl.gov/STAR/system/files/NOTEv9_0.pdf). The Sec. 3.1, Sec. 3.2, and Sec. 3.3 are
 167 for U + U collisions at 193 GeV.

168 The foreground (also called unlike-sign pairs, N_{+-} , including signal and
 169 background) is reconstructed by combining the electron and positron candi-
 170 dates in the same event. The invariant mass (M_{ee}) of the electron pairs are
 171 calculated by Eq. 2,

$$M_{ee} = \sqrt{(E_+ + E_-)^2 - (\vec{p}_+ + \vec{p}_-)^2} \quad (2)$$

172 where $E_{+-} = \sqrt{m_e^2 + \vec{p}_{+-}^2}$, $m_e = 0.511 \text{ MeV}/c^2$ and \vec{p}_{+-} are measured by
 173 the TPC. The signals come from the Drell-Yan production, quarkonia decay,
 174 QGP thermal radiation, heavy flavor semi-leptonic decay, vector mesons in-
 175 medium decay and long-lived hadron decays. The background sources include
 176 the combinatorial background, correlated background and photon conver-
 177 sions. The combinatorial background comes from uncorrelated electron and

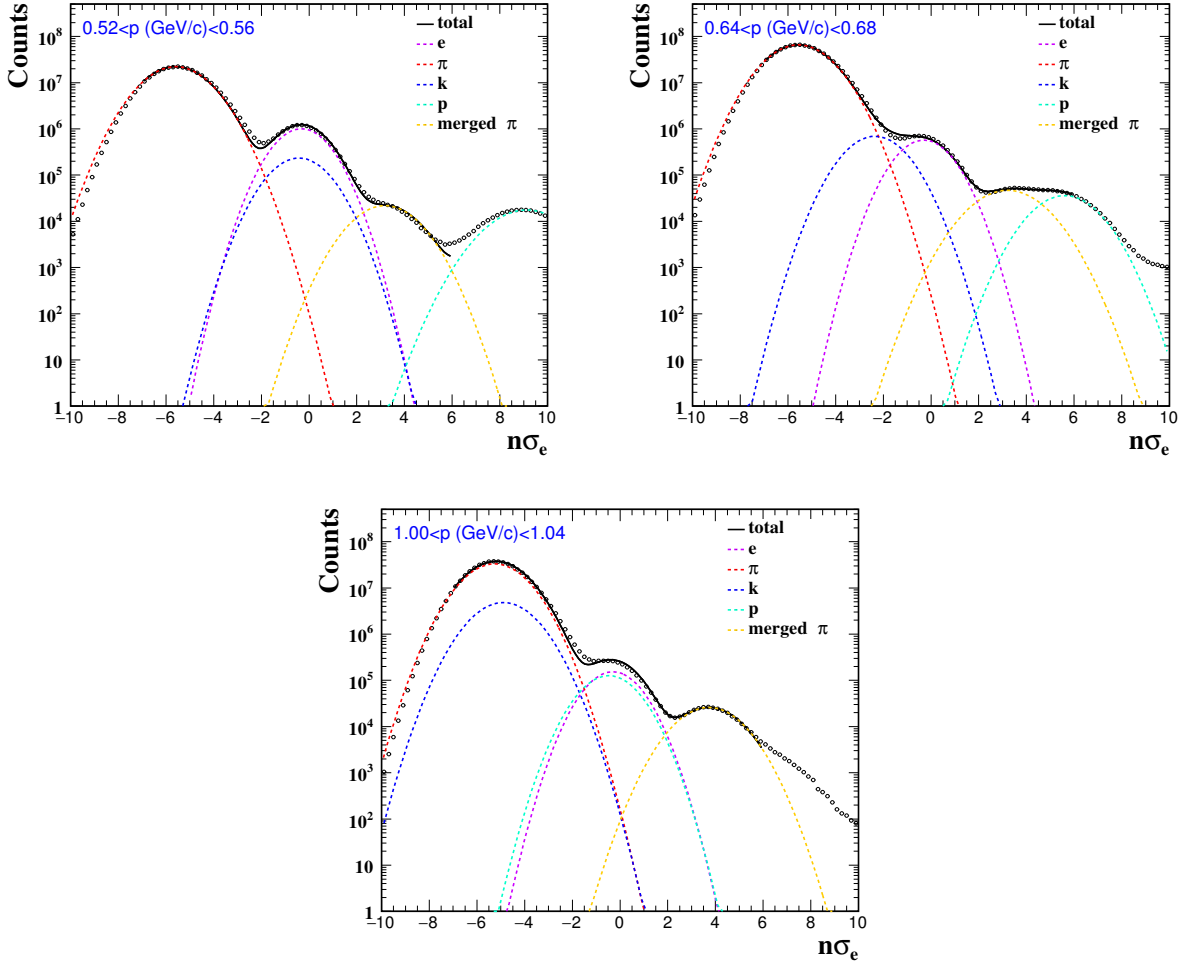


Figure 7: The $n\sigma_e$ distribution after the TOF velocity cut and the multi-Gaussian fit results in three specific momentum bins.

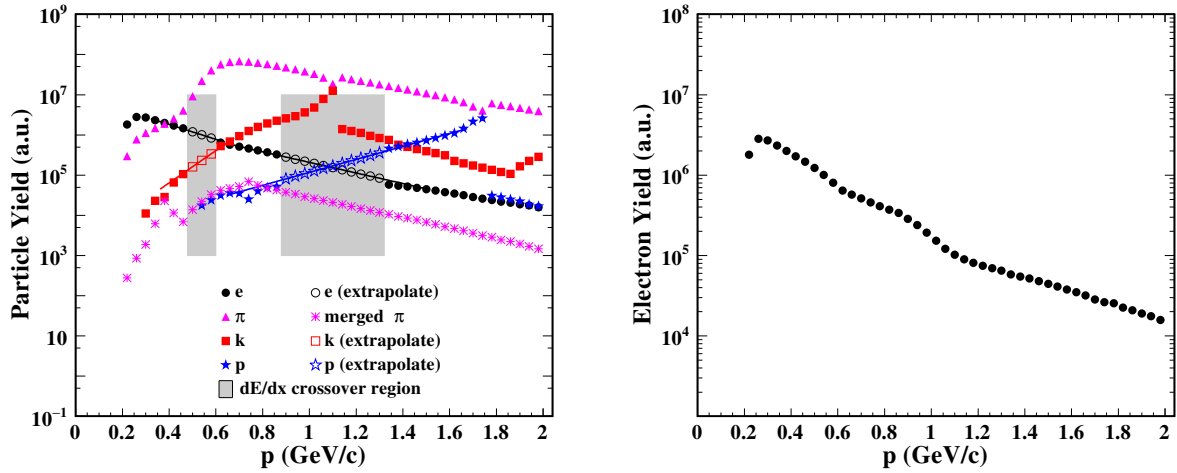


Figure 8: (Left) The yields (solid markers) for different particle species extracted from first-round multi-Gaussian fitting as a function of momentum. The gray areas (left: e/K , right: e/p) depict the dE/dx crossover regions. The solid lines are the exponential fits for extrapolating the hadron yields (open markers) in the crossover regions. (Right) The electron yields (the only free parameter) from the second-round multi-Gaussian fitting to check the fitting reliability.

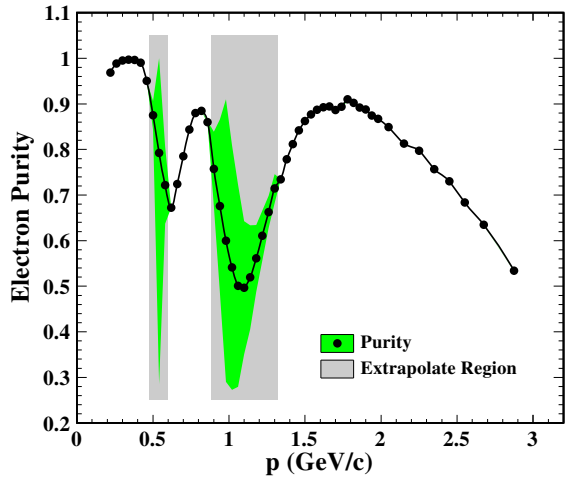


Figure 9: The electron purity in $U + U$ minimum-bias collisions at 193 GeV, the green band represents the systematic uncertainties.

positron pairing while the correlated background comes from correlated electron and positron pairing; for example, pairs from Dalitz decay followed by a conversion of the decayed photon (e.g. $\pi^0 \rightarrow \gamma + e^+ + e^- \rightarrow e^+ + e^- + e^+ + e^-$) or jets (e.g. electron and positron are from same-jet fragmentation or back-to-back di-jet fragmentation). The photon conversion background is from the photon interacting with the detector material and converting into an electron-positron pair. The reconstruction and subtraction of these three background sources are discussed in following sections.

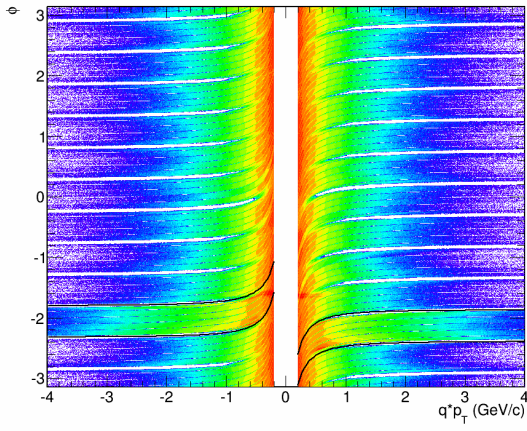


Figure 10: The ϕ vs. p_T distributions for electron and positron candidates. The blank strips are caused by the read-out sector boundaries. The bad TPC sector (sector 7, in positive η region) is constrained by the black solid lines.

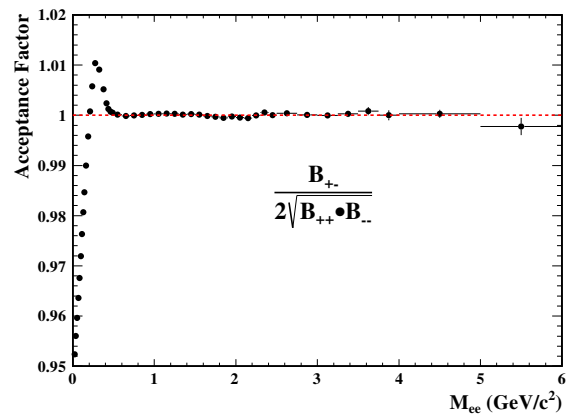


Figure 11: The 1-D acceptance correction factor as a function of M_{ee} in Run12 U + U minimum-bias collisions at 193 GeV.

3.1 Like-sign Technique

The like-sign technique, combining same charge sign electrons into pairs in the same event (N_{++} and N_{--}), is used to account for the combinatorial and correlated backgrounds. The geometric mean of the like-sign pairs $2\sqrt{N_{++} \cdot N_{--}}$, demonstrated in [3], can fully describe the background in the foreground when the e^+ and e^- are produced in statistically independent

¹⁹² pairs. The geometric mean is consistently used in the same-event like-sign
¹⁹³ background reconstruction.

¹⁹⁴ The electrons and positrons are bended into opposite directions owing to
¹⁹⁵ the magnetic field. The ϕ versus p_T of the identified electron and positron
¹⁹⁶ candidates is shown in Fig. 10. The blank strips along the ϕ direction are
¹⁹⁷ caused by the TPC read-out sector boundaries. There is one TPC sector
¹⁹⁸ (sector 7, in positive η region) with dE/dx calibration issue in Run12 U + U
¹⁹⁹ collisions, depicted by the black solid lines in Fig. 10. Thus all the tracks pass-
²⁰⁰ ing through this TPC sector are consistently rejected in this analysis. Due to
²⁰¹ the magnetic field and the TPC de-active areas (read-out sector boundaries,
²⁰² acceptance holes), the acceptances for the unlike-sign and like-sign pairs are
²⁰³ different. The mixed-event technique, discussed in Sec. 3.2, is employed to
²⁰⁴ correct for this effect. The correction factor is calculated by the ratio of the
²⁰⁵ mixed-event unlike-sign and like-sign distribution in each (M_{ee}, p_T^{ee}) bin and
²⁰⁶ applied in 2-dimension (2-D). The final same-event like-sign background used
²⁰⁷ is calculated by the Eq. 3,

$$N_{++\&--}^{corr} = 2\sqrt{N_{++}(M, p_T) \cdot N_{--}(M, p_T)} \times \frac{B_{+-}(M, p_T)}{2\sqrt{B_{++}(M, p_T) \cdot B_{--}(M, p_T)}} \quad (3)$$

²⁰⁸ where N_{++} , N_{--} , B_{++} , and B_{--} represent the distribution of like-sign from
²⁰⁹ the same-event and mixed-event, respectively. B_{+-} represents the distribu-
²¹⁰ tion of unlike-sign from the mixed-event. $N_{++\&--}^{corr}$ denotes the acceptance-
²¹¹ corrected like-sign background from the same-event. Figure 11 shows the 1-D
²¹² acceptance correction factor as a function of M_{ee} in Run12 U + U minimum-
²¹³ bias collisions at 193 GeV.

²¹⁴ 3.2 Mixed-Event Technique

²¹⁵ The like-sign technique, discussed in Sec. 3.1, is taken as the best estima-
²¹⁶ tion for the combinatorial and correlated backgrounds. However, it is limited
²¹⁷ to the statistics. The mixed-event technique, combining the electrons and

positrons from different events with similar characteristics, is used to reproduce the combinatorial background with improved statistical precision. The data sample is divided into different event pools according to the following event level properties: z position of collision vertex, reference multiplicity, and event plane angle. The collision vertex position and reference multiplicity ensure that the same event pool has similar detector acceptance and efficiency. The event plane angle ensures the same event pool has similar momentum phase space alignment, and further guaranteed by the multiplicity assortment to ensure the events have similar momentum phase space distribution. The second-order event plane angle [4, 5] is used to sort the events. The z vertex position, from -30 cm to +30 cm, is divided into 10 equidistant bins. The reference multiplicity is divided into 16 bins (0 - 80%, discussed in Sec. 1) according to the official StRefMult package provided by STAR. The event plane angle Ψ is divided into 24 equidistant bins. This granularity of the event pools is determined by the same procedure discussed in [2]. Each event pool holds 100 events at maximum, and one event in the event pool is randomly updated when the pool is full.

The mixed-event background must be normalized to the acceptance corrected same-event like-sign background. The mixed-event technique can not reproduce the correlated background, thus the normalization factor should be determined in a kinematic region where the same-event like-sign correlated background is negligible. Once the kinematic region selected, the normalization factor and the normalized combinatorial background (B_{+-}^{comb}) are

²⁴¹ calculated via the same method in [3] and also shown in Eq. 4

$$\begin{aligned}
 A_+ &= \frac{\int_{N.R.} N_{++}(M, p_T) dM dp_T}{\int_{N.R.} B_{++}(M, p_T) dM dp_T} \\
 A_- &= \frac{\int_{N.R.} N_{--}(M, p_T) dM dp_T}{\int_{N.R.} B_{--}(M, p_T) dM dp_T} \\
 B_{++}^{norm} &= \int_0^\infty A_+ B_{++}(M, p_T) dM dp_T \\
 B_{--}^{norm} &= \int_0^\infty A_- B_{--}(M, p_T) dM dp_T \\
 B_{+-}^{comb}(M, p_T) &= \frac{2\sqrt{B_{++}^{norm} B_{--}^{norm}}}{\int_0^\infty B_{+-}(M, p_T) dM dp_T} B_{+-}(M, p_T)
 \end{aligned} \tag{4}$$

²⁴² where N.R. represents the normalization region, A_{+-} is the like-sign nor-
²⁴³ malization factor in N.R., $B_{++/-}^{norm}$ is the normalized mixed-event like-sign
²⁴⁴ statistics and B_{+-}^{comb} is the normalized mixed-event unlike-sign distribution.

²⁴⁵ Unfortunately the mixed-event technique, working in Au + Au at 200 GeV,
²⁴⁶ does not work in U + U at 193 GeV. There is no flat kinematic region found to
²⁴⁷ do the normalization, as shown in Fig. 12. This may be related to the asym-
²⁴⁸ metric Uranium geometry compared to the symmetric Gold geometry, shown
²⁴⁹ in Fig. 13. Thus, the same-event like-sign technique is finally used to recon-
²⁵⁰ struct the background in U + U collisions at 193 GeV. **For the very low p_T**
²⁵¹ **dielectron analysis, due to the good signal background ratio, the same-event**
²⁵² **like-sign technique is also consistently used to reproduce the background in**
²⁵³ **Au + Au collisions at 200 GeV.**

²⁵⁴ 3.3 Photon Conversion Removal

²⁵⁵ The photon conversion electron pairs are removed from the foreground
²⁵⁶ using the ϕ_V cut method which is similar to that used by the PHENIX Col-
²⁵⁷ laboration [3]. The opening angle between the electron and positron from
²⁵⁸ the photon conversion should be 0, and the electron and positron are bent
²⁵⁹ only in the plane perpendicular the magnetic field direction which is along

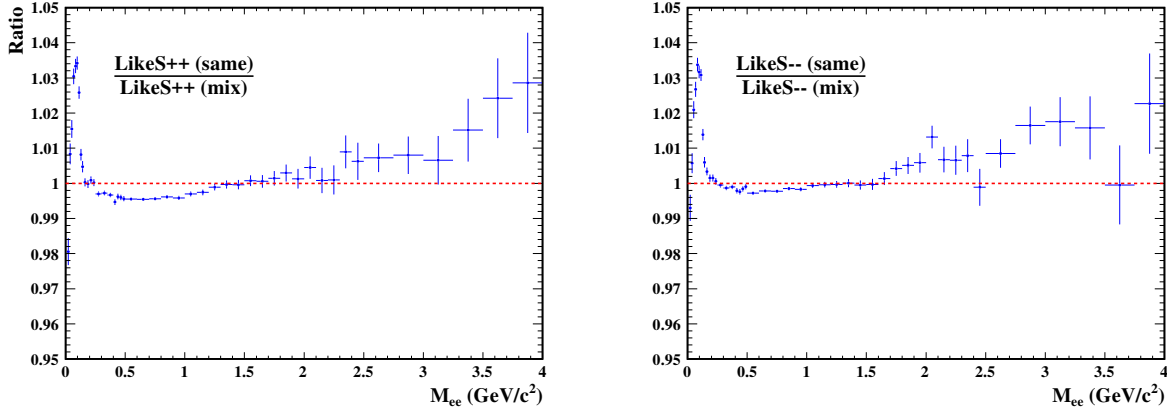


Figure 12: Ratios between same-event and mixed-event like-sign distributions. There is no flat kinematic region to do the mixed-event normalization.

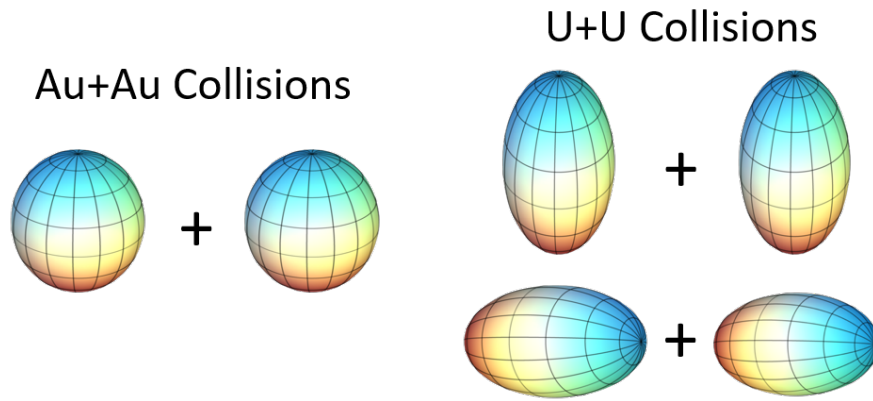


Figure 13: The spherical Gold nuclei (Left) and the ellipsoidal Uranium nuclei (Right).

the beam axis z in STAR. The definitions of the unit vector and ϕ_V angle are shown in the following Eq. 5:

$$\begin{aligned}\hat{u} &= \frac{\vec{p}_+ + \vec{p}_-}{|\vec{p}_+ + \vec{p}_-|}, \quad \hat{v} = \vec{p}_+ \times \vec{p}_- \\ \hat{w} &= \hat{u} \times \hat{v}, \quad \hat{w}_c = \hat{u} \times \hat{z} \\ \cos\phi_V &= \frac{\hat{w}}{|\hat{w}|} \cdot \frac{\hat{w}_c}{|\hat{w}_c|}\end{aligned}\quad (5)$$

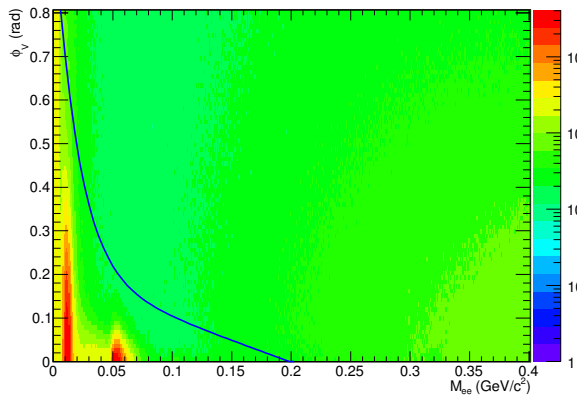


Figure 14: The ϕ_V angle vs. invariant mass distribution in Run12 U + U minimum-bias collisions at 193 GeV. The blue solid curve depicts the mass dependent ϕ_V cut employed to remove the photon conversion electron pairs.

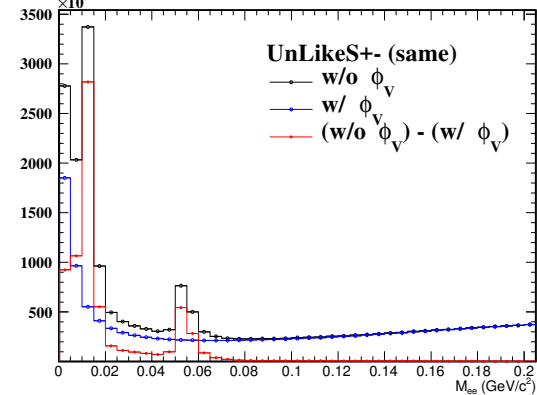


Figure 15: Red: the invariant mass distribution of the photon conversion electron pairs. Black: the unlike-sign distribution without ϕ_V cut. Blue: the unlike-sign distribution with ϕ_V cut.

To illustrate the ϕ_V angle, a little more explanation is added here. Plane A is defined by mother particle momentum direction and beam axis direction, while plane B is defined by the daughter electron, positron momentum directions. The angle between plane A and plane B is defined as ϕ ($0^\circ \leq \phi \leq 90^\circ$). According to Eq. 5, $\phi_V = 90^\circ - / + \phi$. For electron and positron from the photon conversion, $\phi = 90^\circ$, thus the ϕ_V angle is zero or π . A fixed order between electron and positron is used to calculate the ϕ_V in this analysis for avoiding $\phi_V = \pi$. There is no preferred orientation for combinatorial electron and positron pairs, and only very weak dependence for electron and positron

pairs from hadron decays. Figure 14 shows the ϕ_V angle as a function of invariant mass in U + U minimum-bias collisions at 193 GeV. The blue solid curve depicts the mass dependent ϕ_V cut employed to remove the photon conversion electron pairs. Figure 15 shows the invariant mass distribution of the photon conversion electron pairs (red curve). As mentioned before, the different invariant mass peaks depict that the conversion electron pairs are from different materials. The mass shifted from zero is because the electrons are assumed to originate from the primary vertex during the final track reconstruction. Therefore, the two main peaks (for the red histogram) from low to high mass correspond to the conversion from the beam pipe and inner cone support structure, respectively.

3.4 Raw Signals

The background, in this analysis, is subtracted by the same-event like-sign technique. The same-event like-sign distribution is firstly corrected for the acceptance and then subtracted from the inclusive unlike-sign (foreground) distribution. The invariant mass distribution of signal pairs before detector efficiency losses correction (raw signal) is thus obtained. The upper panel of Fig. 16 shows the invariant mass distributions of foreground (black dots), background (black line) and raw signal (blue dots), while the bottom panel shows the signal-to-background ratio in U + U minimum-bias collisions at $\sqrt{s_{NN}} = 193$ GeV. The raw spectra in different p_T bins from various U + U centrality classes are shown in Fig. 17, 18, 19, and 20. The raw spectra of p_T differentials in Run10 Au + Au collisions are shown in Fig. 21, 22, 23, and 24, while that in Run11 Au + Au collisions are shown in Fig. 25, 26, 27, and 28.

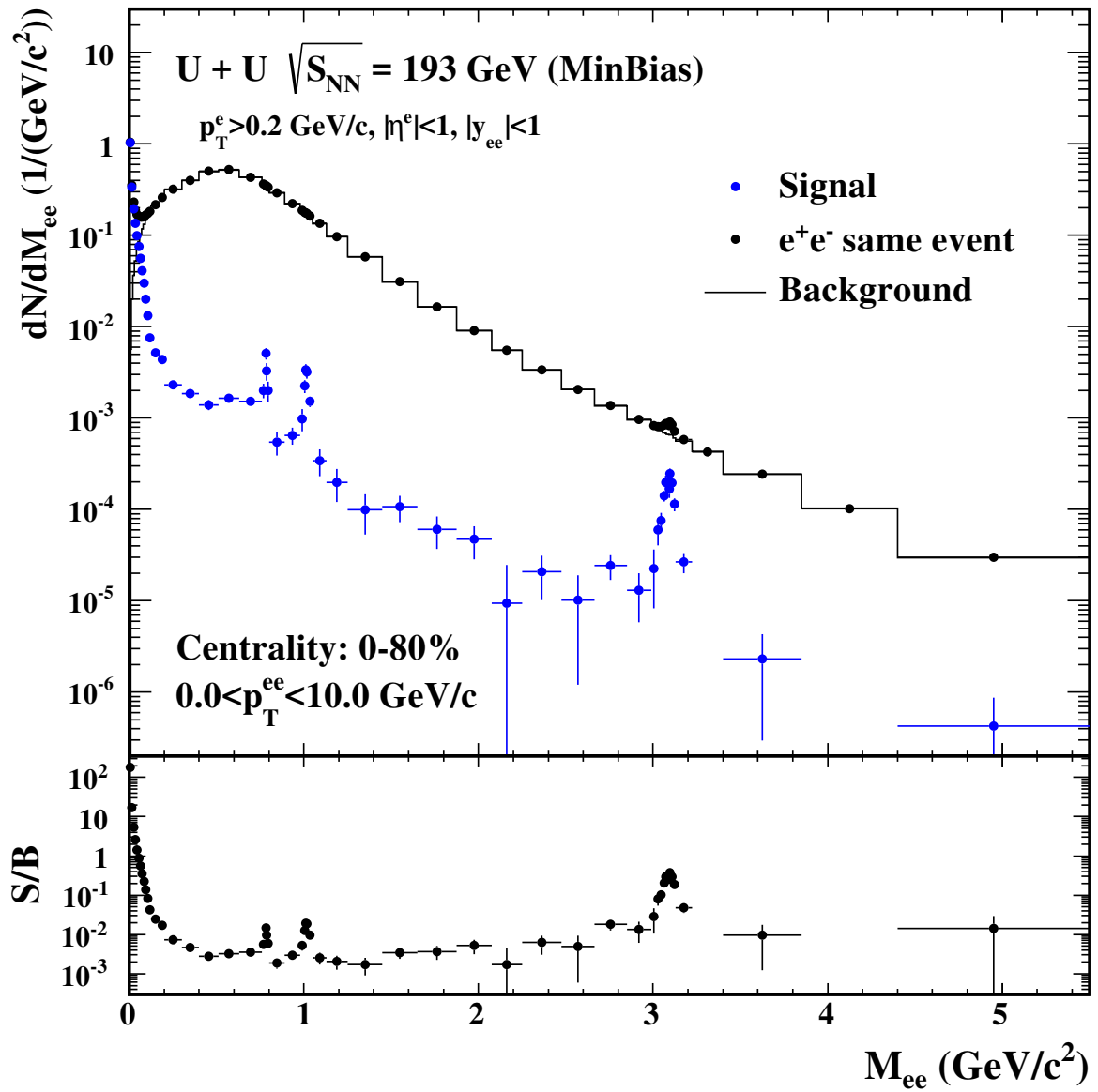


Figure 16: (Top) The invariant mass distributions of raw signal (blue dots), foreground (black dots) and background (black line). (Bottom) The signal-to-background ratio in $U + U$ minimum-bias collisions at $\sqrt{s_{NN}} = 193 \text{ GeV}$.

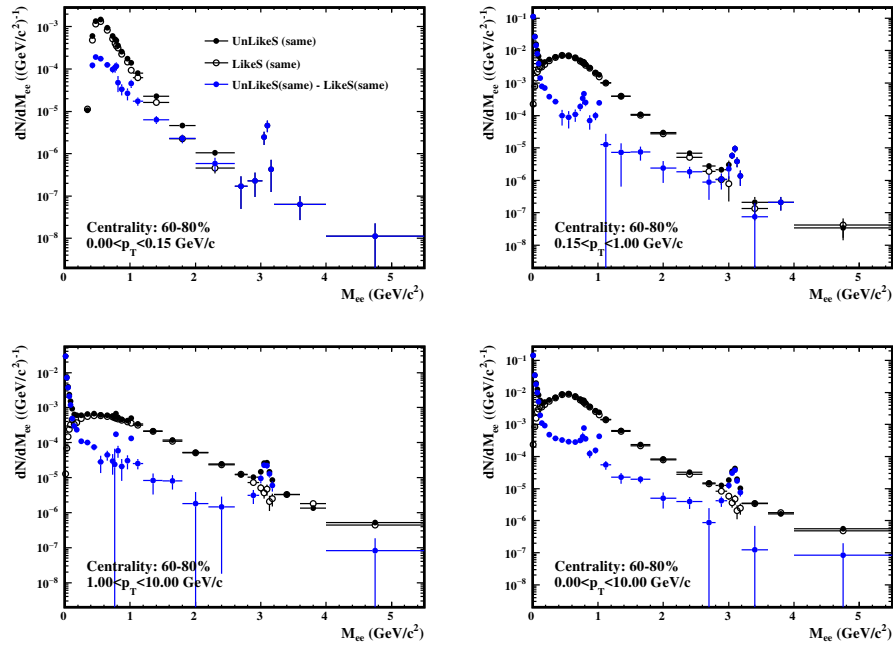


Figure 17: The invariant mass distributions of raw signal (blue dots), foreground (black dots) and background (black open circles) in $U + U$ 60-80% collisions at $\sqrt{s_{NN}} = 193 \text{ GeV}$.

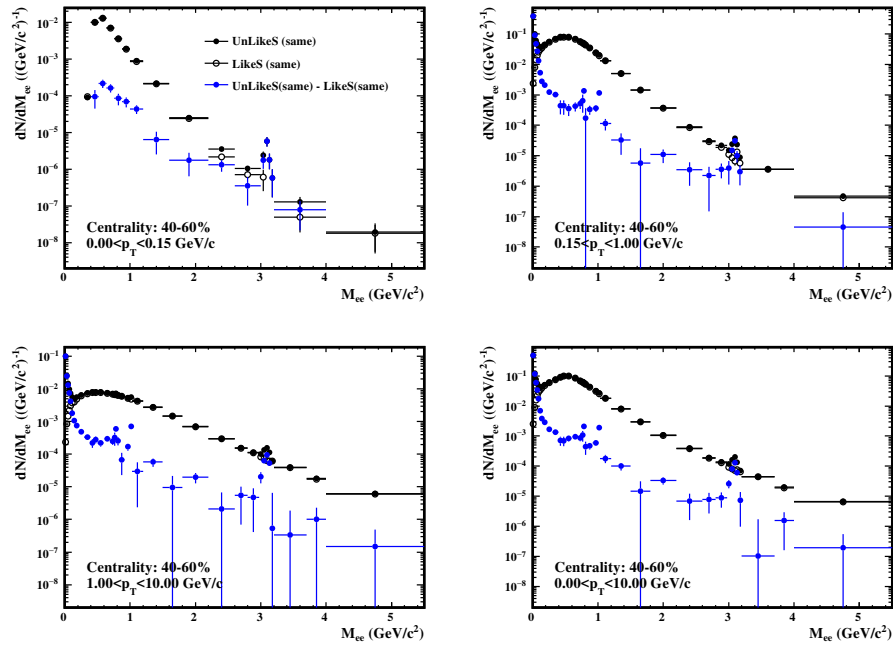
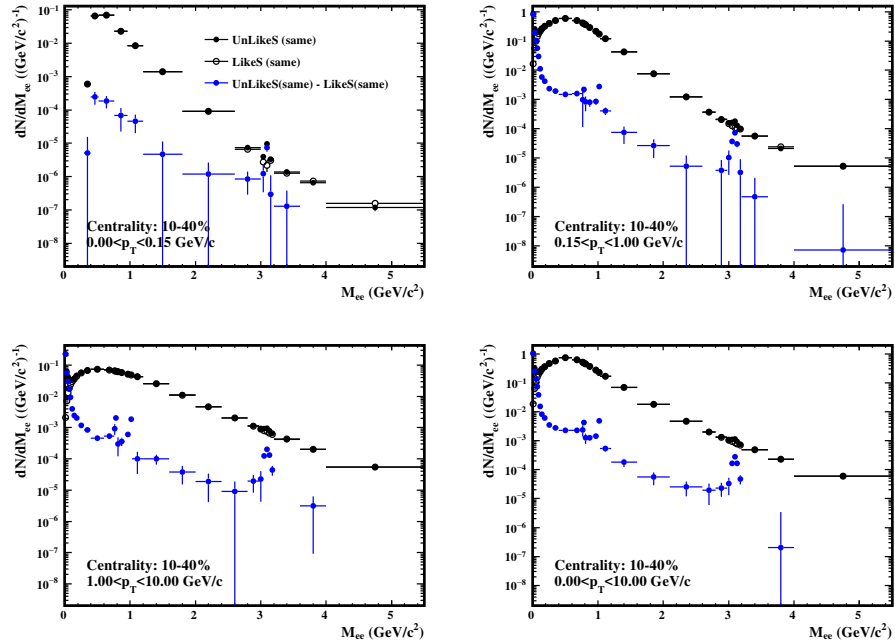
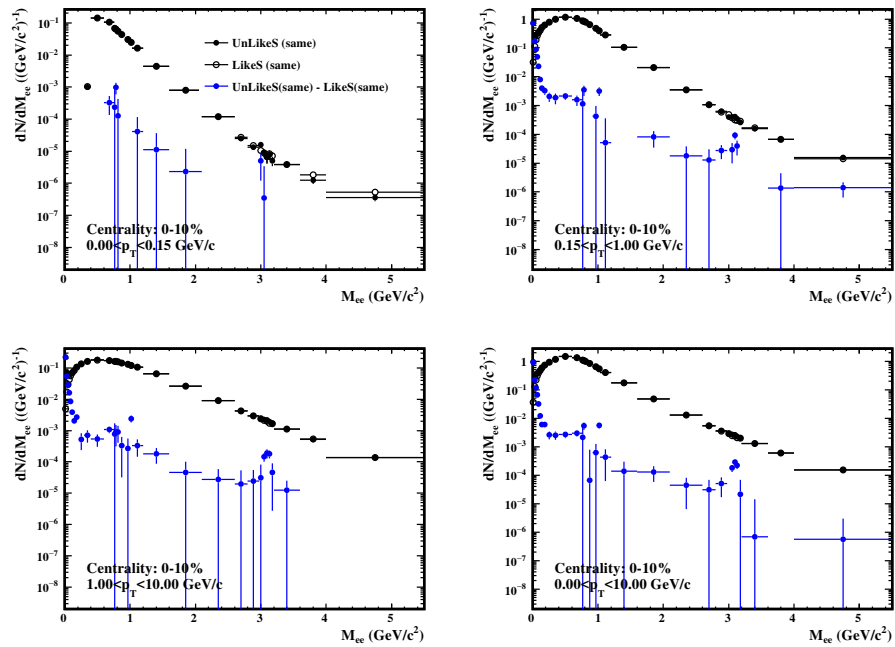


Figure 18: 40-60% $U + U$ collisions at $\sqrt{s_{NN}} = 193 \text{ GeV}$.

Figure 19: 10-40% U + U collisions at $\sqrt{s_{NN}} = 193 \text{ GeV}$.Figure 20: 0-10% U + U collisions at $\sqrt{s_{NN}} = 193 \text{ GeV}$.

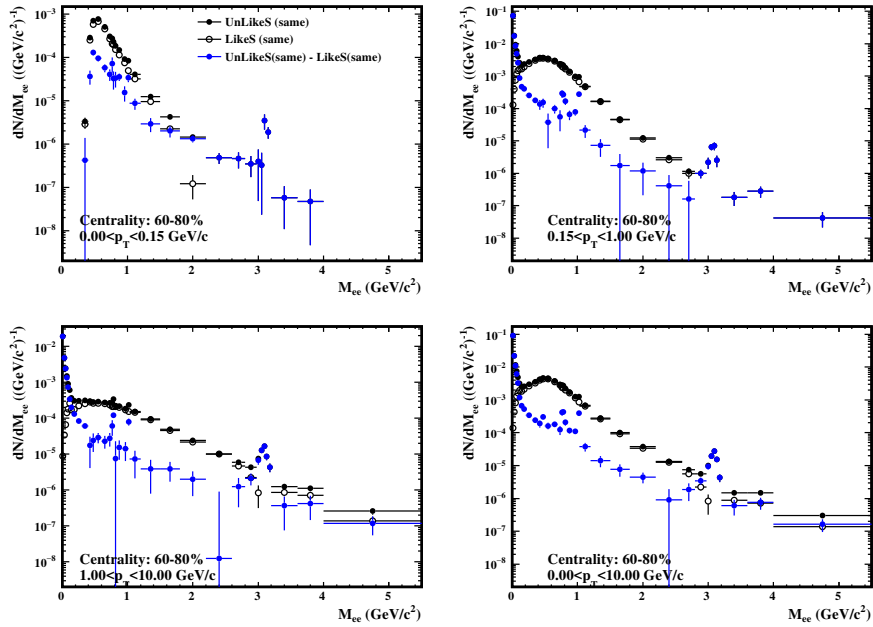


Figure 21: The invariant mass distributions of raw signal (blue dots), foreground (black dots) and background (black open circles) in Run10 Au + Au 60-80% collisions at $\sqrt{s_{NN}} = 200$ GeV.

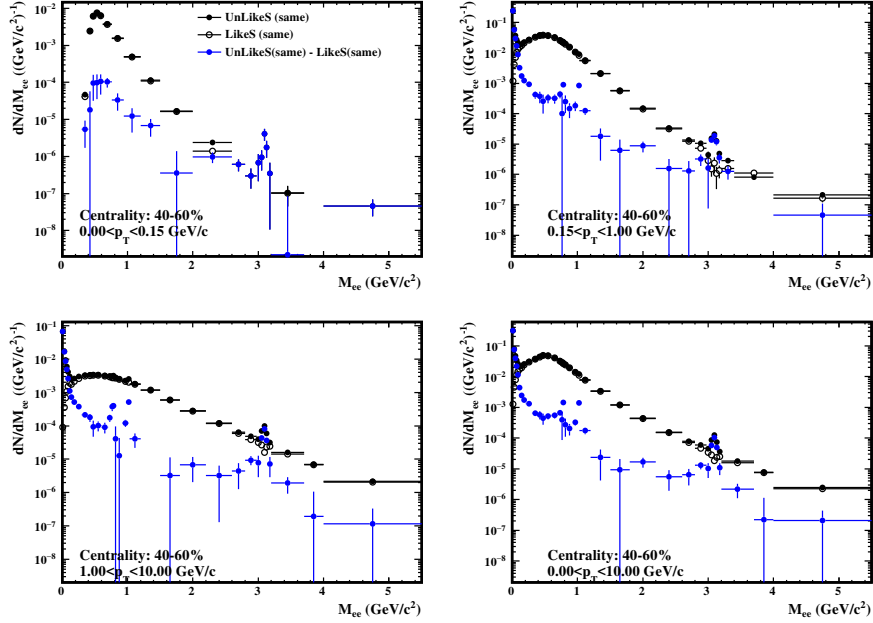
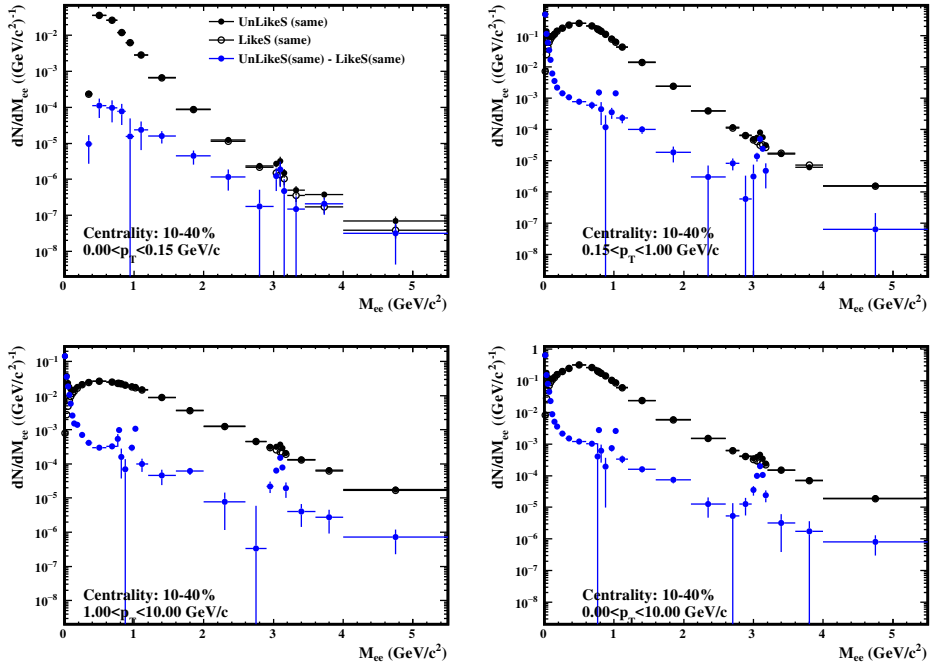
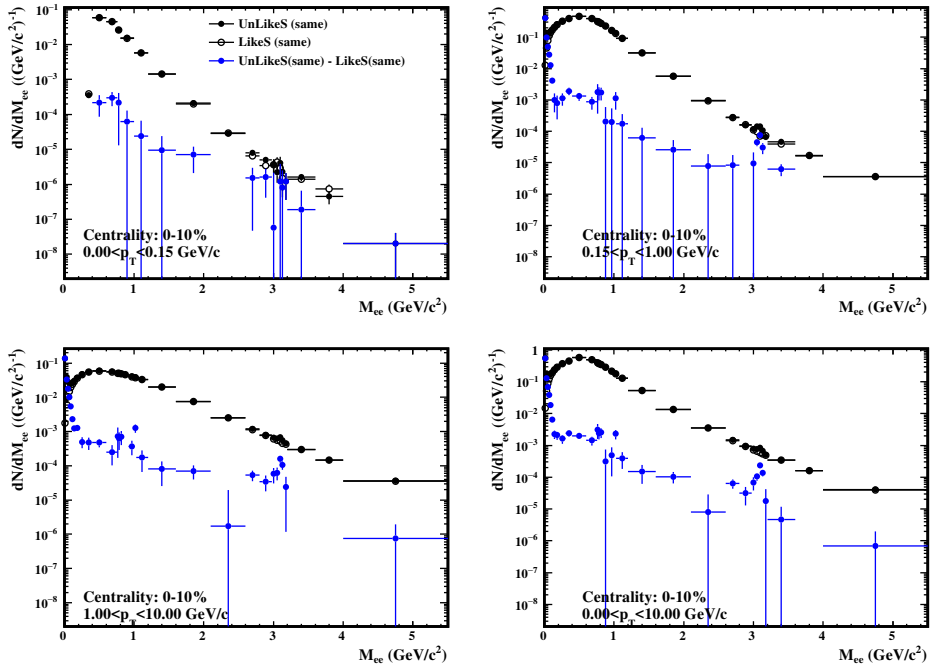


Figure 22: Run10 40-60% central Au + Au collisions at $\sqrt{s_{NN}} = 200$ GeV.

Figure 23: Run10 10-40% central Au + Au collisions at $\sqrt{s_{NN}} = 200$ GeV.Figure 24: Run10 0-10% central Au + Au collisions at $\sqrt{s_{NN}} = 200$ GeV.

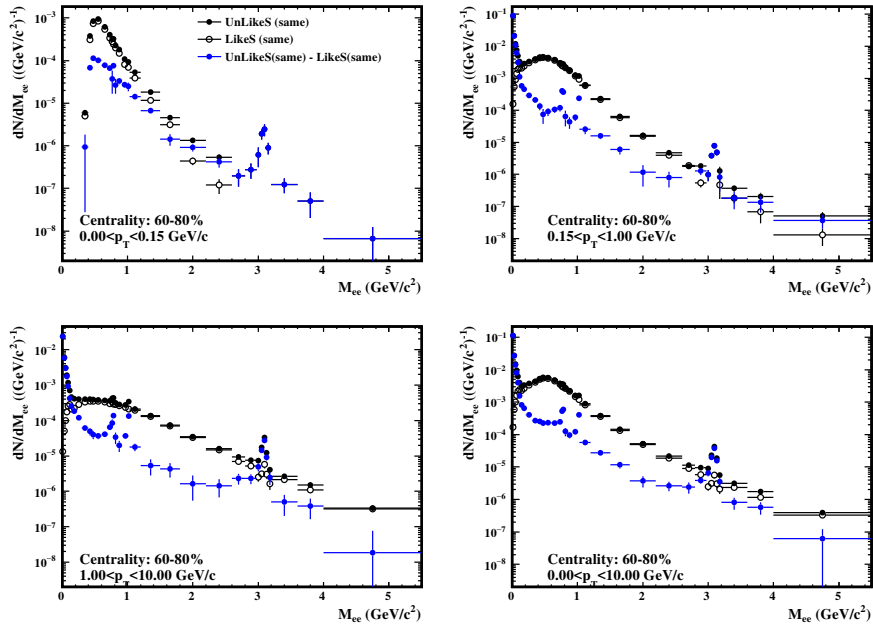


Figure 25: The invariant mass distributions of raw signal (blue dots), foreground (black dots) and background (black open circles) in Run11 Au + Au 60-80% collisions at $\sqrt{s_{NN}} = 200 \text{ GeV}$.

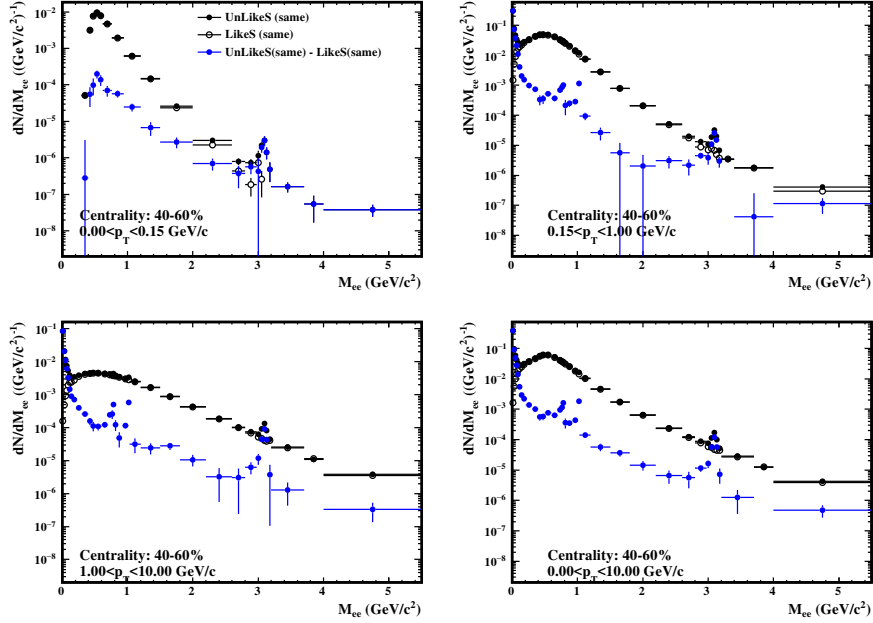


Figure 26: Run11 40-60% central Au + Au collisions at $\sqrt{s_{NN}} = 200 \text{ GeV}$.

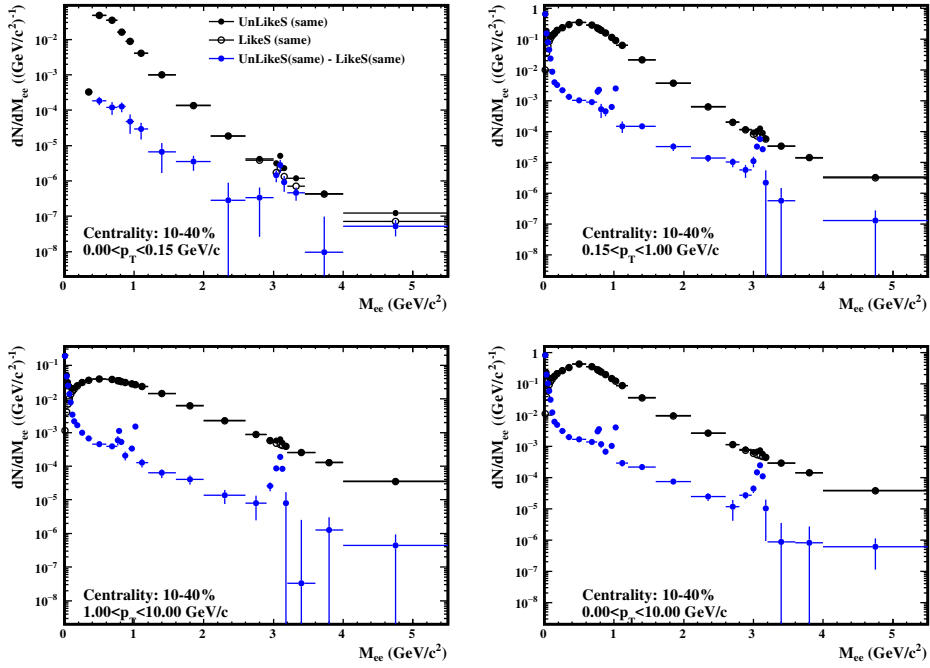


Figure 27: Run11 10-40% central Au + Au collisions at $\sqrt{s_{NN}} = 200$ GeV.

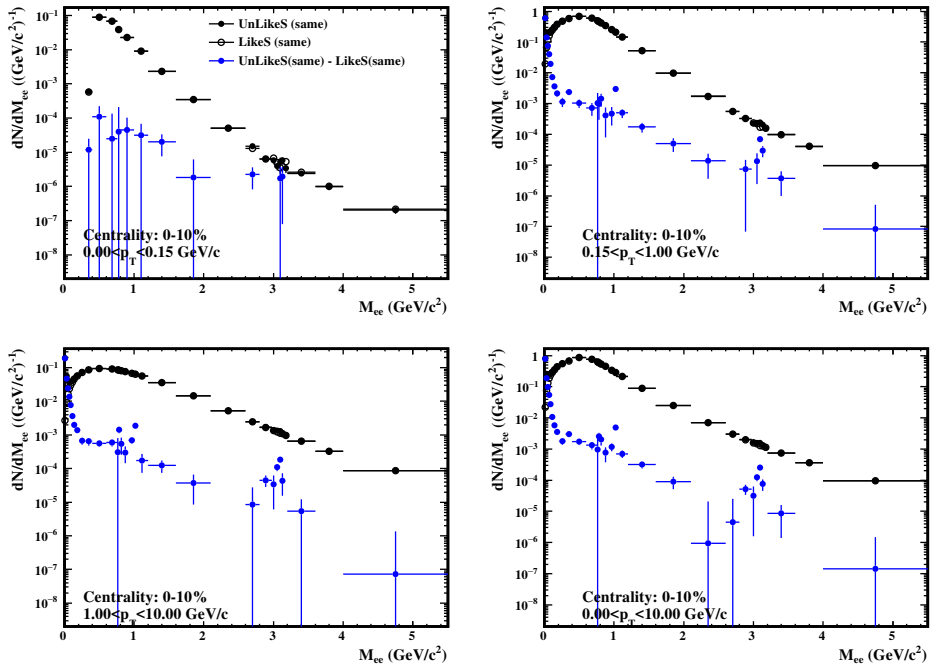


Figure 28: Run11 0-10% central Au + Au collisions at $\sqrt{s_{NN}} = 200$ GeV.

296 4 Efficiency and Acceptance Corrections

297 To obtain the real invariant mass spectrum of dielectron within STAR
 298 acceptance ($p_T^e \geq 0.2 \text{ GeV}/c$, $|\eta_e| \leq 1$, $|Y_{ee}| \leq 1$), the raw spectrum should be
 299 corrected for the efficiency losses. The pair efficiency within STAR acceptance
 300 is evaluated by folding the single track efficiency. To measure the dielectron
 301 excess yield and study the medium properties, the dielectron excess spectrum
 302 (dielectron invariant mass spectrum with hadronic contributions except ρ -
 303 meson subtracted, see details in Sec. 5) is needed to be corrected for the
 304 detector acceptance.

305 4.1 Single Track Efficiency

306 The single track efficiency losses are caused by the detector inefficiency
 307 and electron identification cuts. The detector efficiency includes the TPC
 308 tracking efficiency (ε_{TPC}), nHitsDedx cut efficiency ($\varepsilon_{nHitsDedx}$) and the TOF
 309 matching efficiency (ε_{TOF}). The electron identification cut efficiency (ε_{eID})
 310 includes the efficiencies of TOF velocity and the dE/dx selection cuts. So
 311 the single track efficiency can be derived by the Eq. 6

$$\varepsilon_e = \varepsilon_{TPC} \times \varepsilon_{nHitsDedx} \times \varepsilon_{TOF} \times \varepsilon_{eID} \quad (6)$$

312 The detailed single track efficiency in Au + Au collisions at 200
 313 GeV can be found in p18-p25 (0.4.1 Single track efficiency) of https://drupal.star.bnl.gov/STAR/system/files/NOTEv9_0.pdf

315 NOTE: In Au + Au collisions, the single track efficiencies in
 316 various centrality classes are determined according to the single
 317 track efficiencies in minimum-bias collisions. In U + U collisions,
 318 the single track efficiencies are determined individually for each
 319 centrality class, which are described in detail in following four sub-
 320 sections.

321 **4.1.1 TPC Tracking Efficiency**

322 The TPC tracking efficiency (ε_{TPC}), including the TPC response and ac-
323 ceptance, is evaluated via the standard STAR embedding technique. The
324 Monte Carlo (MC) tracks are embedded into the real data at the raw data
325 level to have a realistic detector occupancy environment. The real data is
326 randomly sampled over the entire U + U minimum-bias data set, while the
327 number of embedded MC tracks is constrained to 5% of the measured mul-
328 tiplicity of the real events to avoid a sizable impact on the realistic TPC
329 tracking efficiency. The MC tracks, with flat p_T , η , and ϕ , are generated and
330 passed through the full simulation of the STAR detector geometry using the
331 GEANT model [6], and then mixed with the real data. The mixed events
332 are processed through the exactly same off-line reconstruction chain as that
333 used in real data production. The quality assurance is made to ensure the
334 MC simulation reproduces the real data before studying the TPC tracking
335 efficiency. The TPC tracking efficiency is derived by taking the ratio of the
336 number of reconstructed MC tracks (N_{rec}), satisfying the track quality cuts
337 except nHitsDedx cut used in this analysis, over the number of embedded
338 MC tracks (N_{emb}), as shown in Eq. 7

$$\varepsilon_{TPC} = \frac{N_{rec} (nHitsFit \geq 20 \& \frac{nHitsFit}{nHitsPoss} \geq 0.52 \& dca \leq 1 \& |\eta| \leq 1)}{N_{emb} (|\eta| \leq 1)} \quad (7)$$

339 The 1-D TPC tracking efficiencies in Run12 U + U collisions at 193 GeV
340 are shown in Fig. 29. However, the 3-D (p_T , η , and ϕ) TPC tracking ef-
341 ficiency will be used in the finally pair efficiency correction, discussed in
342 Sec. 4.2. Detailed information of embedding QA and 3-D TPC tracking ef-
343 ficiencies can be found in [http://www.star.bnl.gov/protected/lfsupc/
344 syang/dielectronPaper/uu193/singleTrkEff/tpcTrkEff/](http://www.star.bnl.gov/protected/lfsupc/syang/dielectronPaper/uu193/singleTrkEff/tpcTrkEff/)

345 **4.1.2 nHitsDedx Cut Efficiency**

346 The nHitsDedx cut efficiency ($\varepsilon_{nHitsDedx}$) is derived from the real data,
347 because the nHitsDedx variable from MC simulation is not consistent with

348 the data. The photonic electron sample (using all track quality and eID cuts
 349 except nHitsDedx and the TOF velocity cuts) is selected according to the
 350 method discussed in Sec. 2.3. The TOF velocity cut is abandoned, because it
 351 biases the nHitsDedx to a large number due to the TOF matching algorithm.
 352 The nHitsDedx cut efficiency is then derived by comparing the number of
 353 photonic electron tracks with and without nHitsDedx cut. Figure 30 shows
 354 the nHitsDedx cut efficiencies as a function of p_T in Run12 U + U collisions
 355 at 193 GeV.

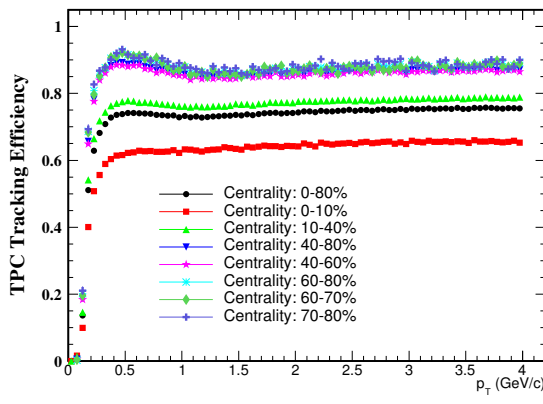


Figure 29: The 1-D TPC tracking efficiencies in Run12 U + U minimum-bias and different centrality collisions at 193 GeV.

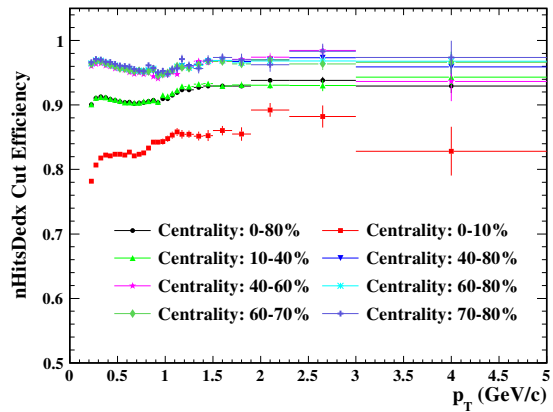


Figure 30: The nHitsDedx cut efficiency in Run12 U + U minimum-bias and different centrality collisions at 193 GeV.

356 4.1.3 TOF Matching Efficiency

357 The TOF matching efficiency (ε_{TOF}), including the TOF response and the
 358 acceptance difference between the TPC and TOF, is evaluated by the real
 359 data. It can be calculated by comparing the number of qualified primary
 360 tracks matched with the TOF (with $\beta > 0$, $N_{matched}$) over the number of
 361 qualified primary tracks (N_{TPC}). Due to the limited statistics of pure electron
 362 sample, the pure pion sample selected by a tight TPC dE/dx cut ($|n\sigma_\pi| <$
 363 0.6), is thus used to generate the 3-D (p_T , η , and ϕ) TOF matching efficiency.
 364 The TOF matching efficiency difference between the electron and pion is then

corrected for each (η, ϕ) bin using the same p_T dependent correction factor. The TOF matching efficiency difference between electrons and pions, is due to the decay loss of pions between the TPC and TOF as well as other effects (e.g. pile-up effect). The 1-D TOF matching efficiency and the p_T dependent correction factor in Run12 U + U collisions at 193 GeV are shown in Fig. 31. The centrality dependence of correction factor is shown in Fig. 32. 3-D TOF matching efficiencies can be find in <http://www.star.bnl.gov/protected/lfsupc/syang/dielectronPaper/uu193/singleTrkEff/tofMatchEff/>.

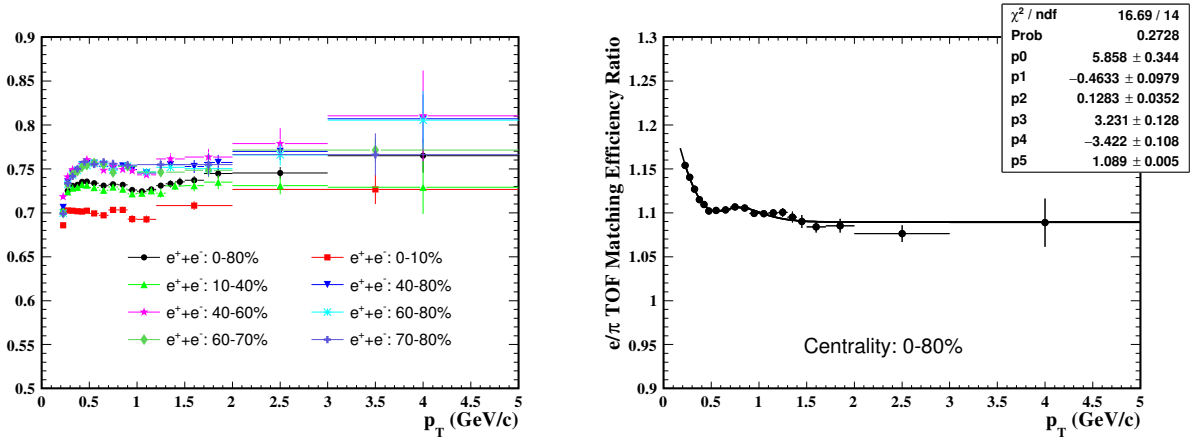


Figure 31: (Left) Centrality dependence of 1-D TOF matching efficiency for pure electron and pion sample in Run12 U + U collisions at 193 GeV. (Right) The corresponding TOF matching efficiency ratio of electron over pion as a function of p_T in Minimum-bias U + U collisions.

4.1.4 eID Cuts Efficiency

The electron identification cut efficiency (ε_{eID}) includes two components: the TOF velocity ($1/\beta$) cut efficiency and dE/dx cut ($n\sigma_e$) efficiency. Pure electron sample is used to evaluate the TOF velocity cut efficiency, and the $1/\beta$ distribution of the pure electron is shown in the left panel of Fig. 33. The red lines depict the $1/\beta$ cut used in this analysis, and the efficiency is calculated using two methods: Gaussian fitting and bin counting. The Gaussian fitting method overestimates the $1/\beta$ cut efficiency due to the tail

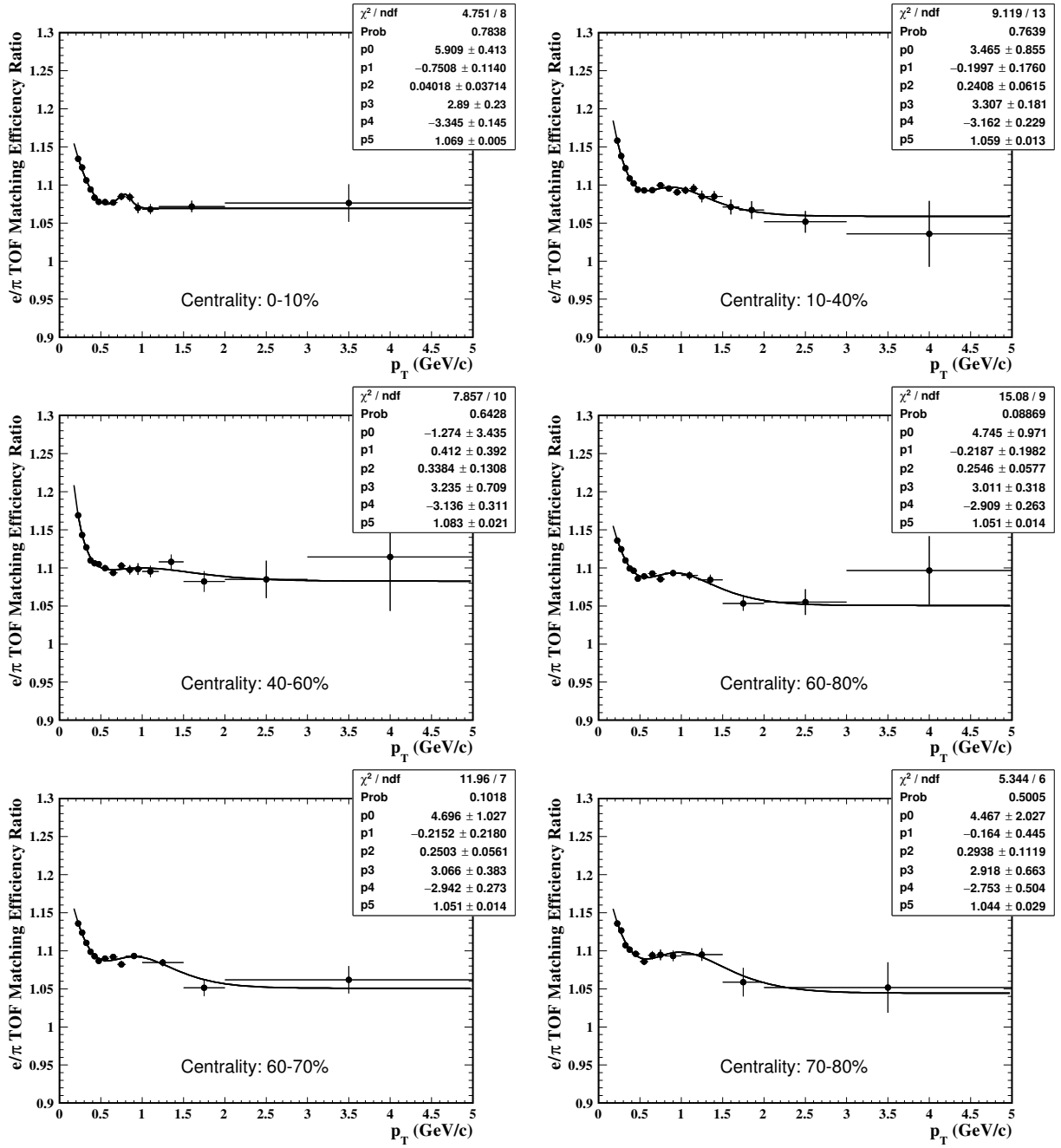


Figure 32: Centrality dependence of TOF matching efficiency ratio of electron over pion.

structure in each p_T bin. Thus the default $1/\beta$ cut efficiency value, shown in the right panel (blue circles) of Fig. 33 and Fig. 34, comes from the bin counting method, and the difference between this two methods is taken into account for the systematic uncertainty. The $n\sigma_e$ cut efficiency is derived from the multi-Gaussian fit discussed in Sec. 2.3. Figure 35 depicts the $n\sigma_e$ cut efficiency in Run12 U + U collisions at 193 GeV.

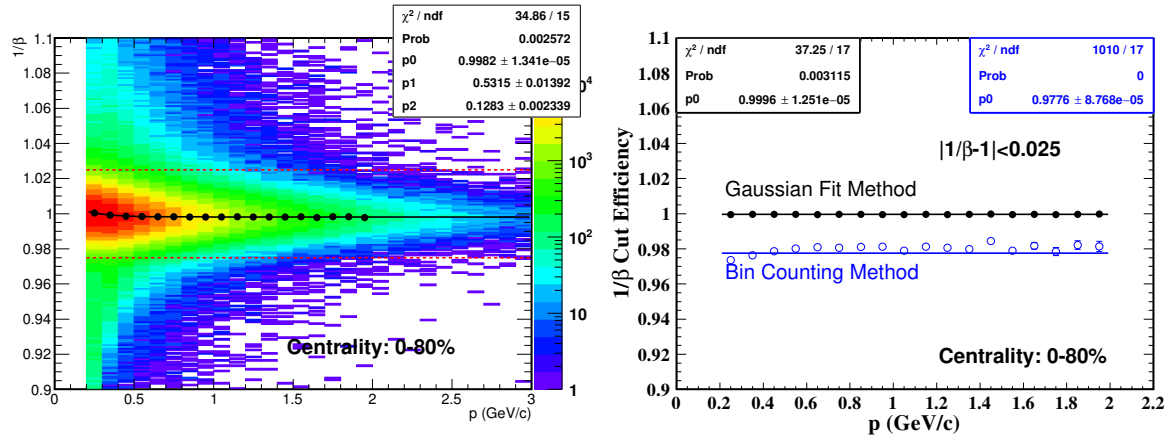


Figure 33: (Left) The $1/\beta$ distribution for pure electron sample in Run12 U + U minimum-bias collisions at 193 GeV. Red dashed lines represent the $1/\beta$ cut used in this analysis. Black dots represent the $1/\beta_{mean}$ for each p_T bin while the black curve is the fit function. (Right) The $1/\beta$ cut efficiencies using bin counting (default, blue circles) and Gaussian fit (black dots) methods.

4.2 Pair Efficiency

The dielectron pair efficiency within STAR acceptance ($p_T^e \geq 0.2$ GeV/ c , $|\eta_e| \leq 1$, $|Y_{ee}| \leq 1$) is evaluated from single track efficiency by two different simulation folding methods:

- (i) Toy MC simulation (Virtual photon simulation), which uses the virtual photon as input. The 2-D kinematics (M_{ee}, p_T) of the virtual photon is taken from the hadronic cocktail (discussed in Sec. 5) with flat rapidity (Y), azimuthal (ϕ) distribution, and the virtual photon decays into electron and positron pairs isotropically.

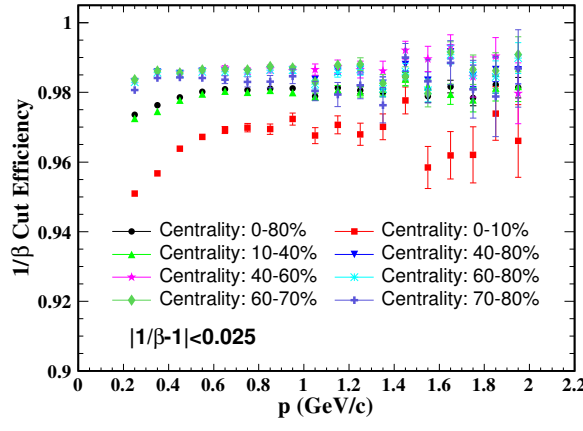


Figure 34: Centrality dependence of $1/\beta$ cut

efficiencies using bin counting method in $U + U$ collisions at 193 GeV.

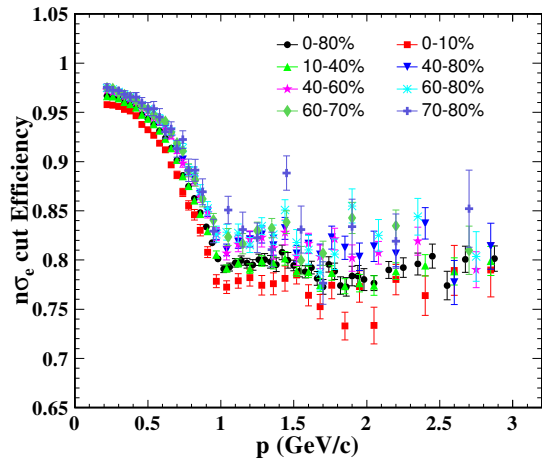


Figure 35: The $n\sigma_e$ cut efficiency in $U + U$ collisions at 193 GeV.

396 (ii) Cocktail simulation, which uses the hadronic cocktail as input, including
 397 the correlated heavy flavor decay ($c\bar{c}$, $b\bar{b}$) and Drell-Yan process from
 398 PYTHIA [7] simulation. The long-lived hadrons decay into electron and
 399 positron pairs isotropically. However, the electron and position from the
 400 heavy flavor decay are highly correlated.

401 The largest difference between these two methods is the correlated heavy
 402 flavor contribution, which is still unclear in heavy-ion collisions due to possible
 403 medium modifications of the heavy flavor correlations compared to those in
 404 $p + p$ collisions. In this analysis, the heavy flavor correlations rely on the
 405 PYTHIA simulation without any artificial modification.

406 The single track efficiencies caused by the TPC tracking and TOF match-
 407 ing are folded into pair efficiency in 3-D (p_T , η , and ϕ) momentum space while
 408 the others are folded in 1-D (p_T) momentum space. The momentum resolu-
 409 tion and energy loss effects, discussed in Sec. 5, are also taken into account
 410 during the folding process. The pair efficiency is calculated and applied in 2-D
 411 kinematics (M_{ee} , p_T). Figure 36 shows the 2-D pair efficiency evaluated by the
 412 “Virtual Photon simulation” and “Cocktail simulation” methods in Run12 U
 413 + U minimum-bias collisions at 193 GeV (The 2-D pair efficiencies for other

centralities in U + U collisions can be found in <http://www.star.bnl.gov/protected/lfsupc/syang/dielectronPaper/uu193/pairEff/>). Figure 37 shows the p_T integrated ($0 < p_T < 5 \text{ GeV}/c$) and very low p_T ($p_T < 0.15 \text{ GeV}/c$) 1-D pair efficiency comparisons between these two methods in various centrality classes, and the differences are pretty small. The default pair efficiency is evaluated by the “Virtual Photon simulation” and the difference between these two methods is taken into account for systematic uncertainty. Figure 38 and Fig. 39 show the p_T integrated ($0 < p_T < 5 \text{ GeV}/c$) and very low p_T ($p_T < 0.15 \text{ GeV}/c$) 1-D pair efficiency determined by ”Virtual Photon” method in various centrality classes of Run10 and Run11 Au + Au collisions at 200 GeV, separately. The 2-D pair efficiencies for various centralities in Au + Au collisions can be found in <http://www.star.bnl.gov/protected/lfsupc/syang/dielectronPaper/auau200/pairEff/>

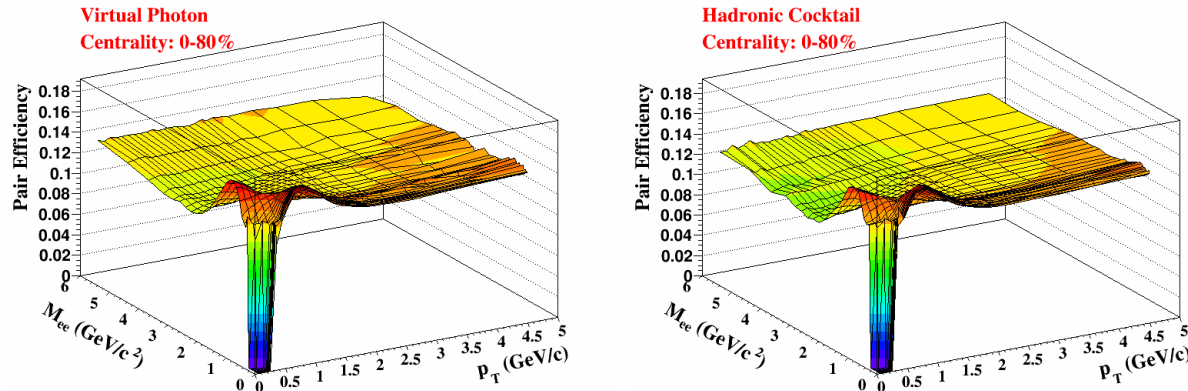


Figure 36: The 2-D pair efficiency evaluated by the “Virtual photon simulation” (Left) and “Cocktail simulation” (Right) methods in Run12 U + U minimum-bias collisions at 193 GeV.

The pair efficiencies have been also evaluated by using the $\gamma\gamma \rightarrow e^+e^-$ interaction as input. In which, the pair efficiencies are compatible with that obtained from ‘Virtual Photon simulation’, demonstrating the pair efficiency within STAR acceptance ($p_T^e \geq 0.2 \text{ GeV}/c$, $|\eta_e| \leq 1$, $|Y_{ee}| \leq 1$) evaluated by folding method is not sensitive to the underlying physics mecha-

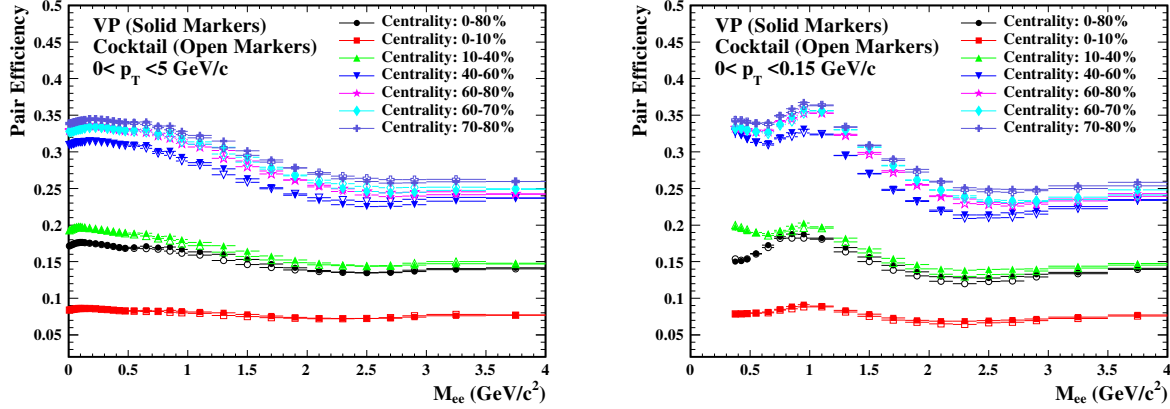


Figure 37: The p_T integrated (Left) and very low p_T (Right) 1-D pair efficiency comparisons between the “Virtual photon simulation” (Solid Markers) and “Cocktail simulation” (Open Markers) for different centralities in Run12 U + U collisions at 193 GeV..

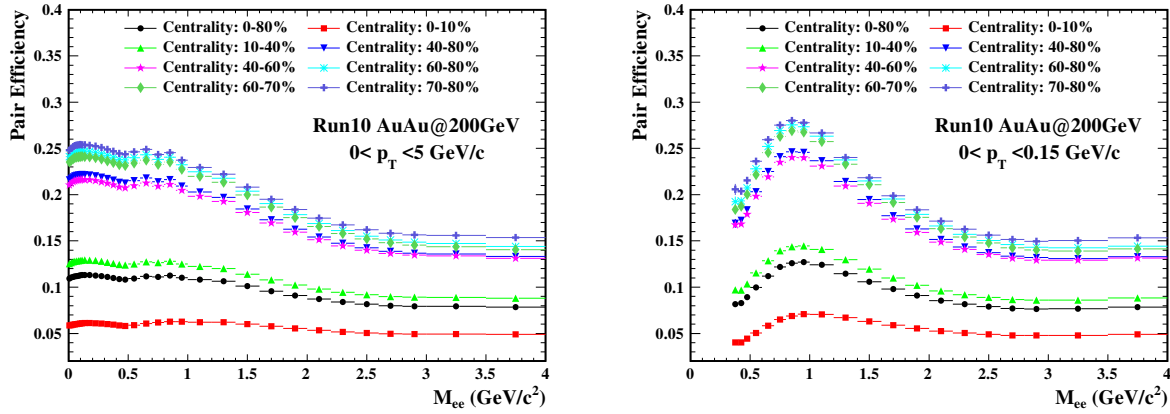


Figure 38: Centrality dependence of p_T integrated (Left) and very low p_T (Right) 1-D pair efficiency in Run10 Au + Au collisions at 200 GeV.

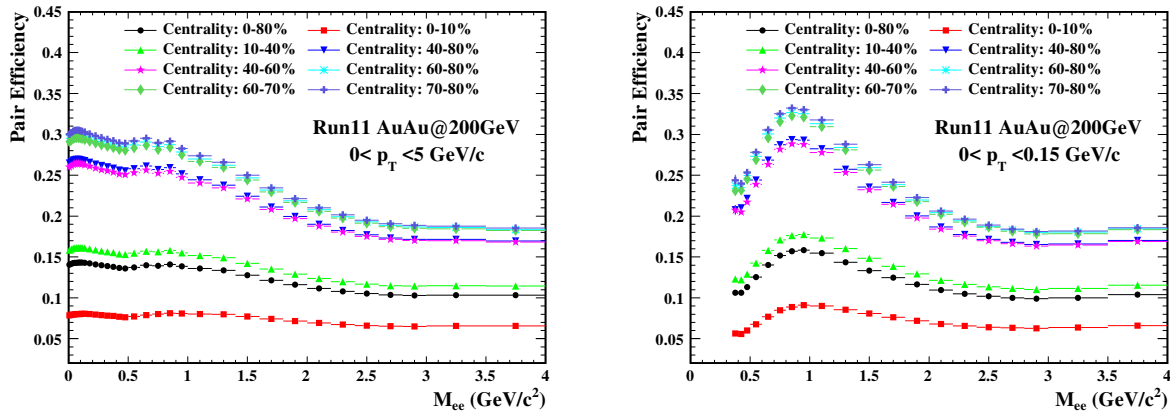


Figure 39: Centrality dependence of p_T integrated (Left) and very low p_T (Right) 1-D pair efficiency in Run11 Au + Au collisions at 200 GeV.

nisms. The pair efficiency comparisons can be found in Fig. 40. The detailed discussions for the Virtual Photon simulation” and ” $\gamma\gamma \rightarrow e^+e^-$ simulation” can be found in http://www.star.bnl.gov/protected/lfsupc/syang/dielectronPaper/lowPtWebPage/SupportingDoc/20171108_Efficiency_CrossCheck_VPvsGammaGamma.pdf

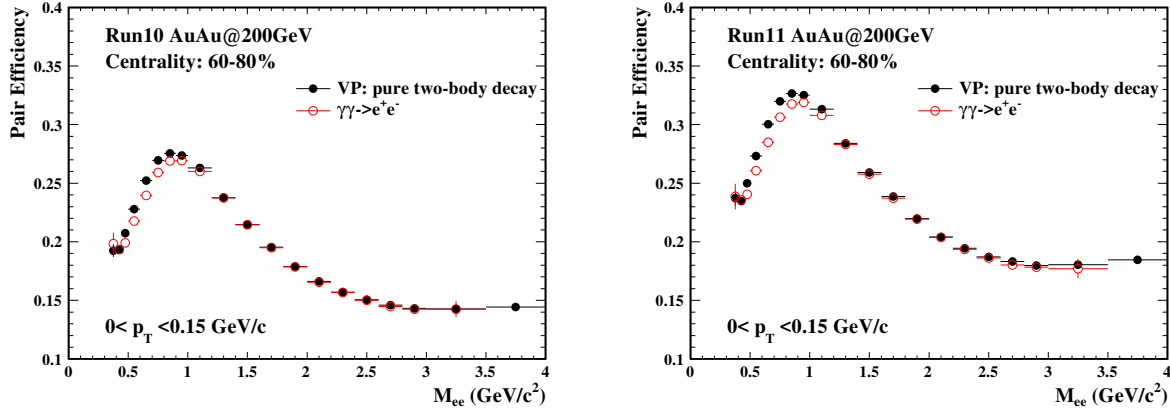


Figure 40: The comparison of pair efficiencies obtained from “Virtual photon simulation” and ” $\gamma\gamma \rightarrow e^+e^-$ simulation” methods in Run10 (Left) and Run11 (Right) Au + Au minimum-bias collisions at 200 GeV.

The ϕ_V cut (reject electron pairs) efficiency is evaluated through π^0 Dalitz decay embedding (see Sec. 4.1.1) and the virtual photon simulation. The

⁴³⁹ ϕ_V cut efficiency obtained by these two methods is shown in Fig. 41. The
⁴⁴⁰ default ϕ_V cut efficiency is evaluated by the virtual photon simulation and the
⁴⁴¹ difference between these two methods is taken into account for the systematic
⁴⁴² uncertainty. **The ϕ_V cut, which is only applied in $M_{ee} < 0.2 \text{ GeV}/c^2$,**
⁴⁴³ **has no effect at all for the very low $p_T e^+e^-$ analysis.**

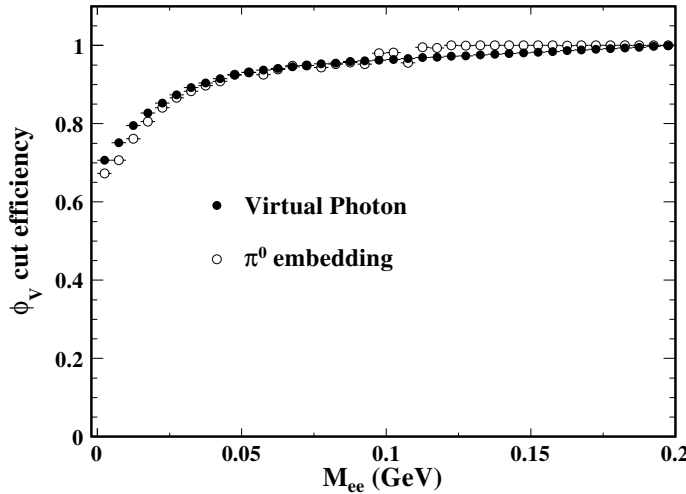


Figure 41: The ϕ_V angle cut efficiencies obtained by π^0 Dalitz decay embedding and virtual photon simulation.

⁴⁴⁴ 5 Hadronic Cocktail Simulation

⁴⁴⁵ Dielectrons as measured by the detector originate from all stage in the
⁴⁴⁶ evolution of heavy-ion collisions. The contribution of the dielectron pairs from
⁴⁴⁷ hadronic decays, so called hadronic cocktail, to the final dielectron spectrum
⁴⁴⁸ can be well evaluated through MC simulation once their yields and p_T spectra
⁴⁴⁹ are measured. The components of the cocktail simulation in this analysis are
⁴⁵⁰ listed below:

- ⁴⁵¹ (i) Two-body decays: $\omega \rightarrow e^+e^-$, $\phi \rightarrow e^+e^-$, $J/\psi \rightarrow e^+e^-$, $\psi' \rightarrow e^+e^-$.
- ⁴⁵² (ii) Dalitz decays: $\pi^0 \rightarrow \gamma e^+e^-$, $\eta \rightarrow \gamma e^+e^-$, $\eta' \rightarrow \gamma e^+e^-$, $\omega \rightarrow \pi^0 e^+e^-$,
- ⁴⁵³ $\phi \rightarrow \eta e^+e^-$.

454 (iii) Heavy-flavor decays: $c\bar{c} \rightarrow e^+e^- + X$, $b\bar{b} \rightarrow e^+e^- + X$.

455 (iv) Drell-Yan process.

456 The ρ^0 , considered to be modified by the hadronic medium, is excluded in
457 the cocktail simulation.

458 For U + U collisions at 193 GeV, there is no measurement for the identified
459 particle species. However, the energy density created in U + U collisions at
460 $\sqrt{s_{NN}} = 193$ GeV is only about 20% higher than that in Au + Au collisions
461 at $\sqrt{s_{NN}} = 200$ GeV [8]. Thus the hadron p_T spectra in Au + Au collisions
462 at 200 GeV [2] are employed for cocktail simulation in this analysis, as shown
463 in Fig. 42. The measurements of identified particle species (the symbols in
464 Fig. 42) except J/ψ in Au + Au collisions at 200 GeV, are simultaneously
465 fitted by a core-corona-based Tsallis Blast-Wave (TBW) model [9, 10]. The
466 core and corona describe the bulk production and the hard scattering con-
467 tributions from $p + p$ -like collisions, respectively. The J/ψ is excluded from
468 simultaneously fit, because the J/ψ is not considered as a component of the
469 bulk medium. The TBW fit can well describe the measured light hadron
470 spectra and also provide predictions for the meson species without measure-
471 ment (e.g. p_T spectra of all the input meson species in $p_T < 0.15$ GeV/c)
472 using the same core TBW parameters obtained from the simultaneously fit.
473 The rapidity and azimuthal distribution of the input hadron are assumed to
474 be flat. The yields (dN/dy) of the input hadron in Au + Au collisions are
475 extracted by integrating the fits over the whole p_T region.

476 The dN/dy or cross section (σ) with their uncertainties and correspond-
477 ing decay branching ratios of various cocktail components used in Au + Au
478 minimum-bias collisions at 200 GeV, are summarized in [2] (TABLE III).
479 The dN/dy of cocktail hadron components (without measurements) used in
480 U + U minimum-bias collisions at 193 GeV are essentially derived from that
481 of Au + Au minimum-bias collisions at 200 GeV by N_{part} . The π^0 dN/dy
482 ($(\pi^+ + \pi^-)/2$) [11] of Au + Au collisions at 200 GeV scaled by $N_{part}/2$ as

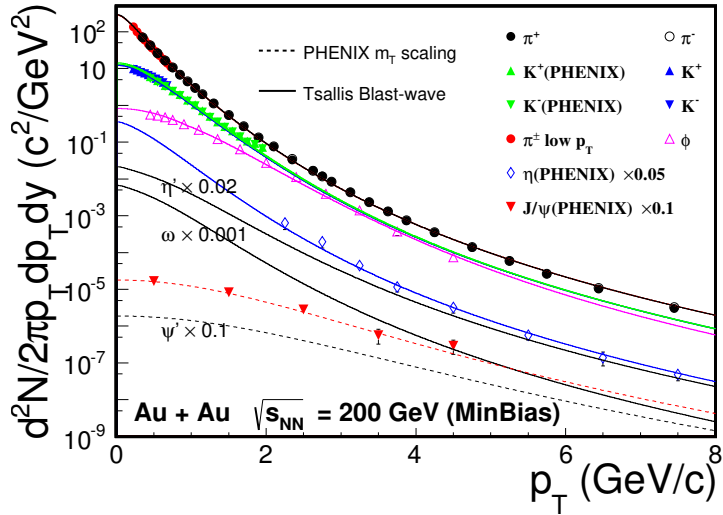


Figure 42: The invariant yields of mesons in Au + Au collisions at 200 GeV. The solid lines show the simultaneous TBW fit to the measured data points (except J/ψ) and the TBW predictions for η , η' , and ω with the same core TBW parameters. The dashed lines show the TBW fit to the measured J/ψ and the prediction for the ψ' .

a function of N_{part} , is fitted by a first-order polynomial function. The π^0 dN/dy of U + U collisions at 193 GeV for different centralities are evaluated by this first-order polynomial function, as shown in Fig. 43. The input dN/dy for other cocktail hadron components (except J/ψ and ψ') in U + U minimum-bias collisions at 193 GeV are scaled with the relative pion yields, R_{π^0} (shown in Tab. 5), with respect to Au + Au minimum-bias collisions at 200 GeV. The dN/dy of J/ψ and ψ' are scaled by relative N_{coll} . The quoted systematic uncertainties of the hadron yields are the same as that of Au + Au collisions at 200 GeV. The input p_T spectra of cocktail hadron components for different centralities in U + U collisions at 193 GeV, are also the same as those (using the similar TBW function fit to the available data) of the corresponding centralities in Au + Au collisions at 200 GeV. The heavy flavor contributions to the hadronic cocktail will be discussed later.

Once the kinematics (p_T , η , and ϕ) of the parent hadron obtained, the kinematics of the daughter electrons are determined by the decay kinematics. The electron pair mass depends on the parent particle and the decay mode

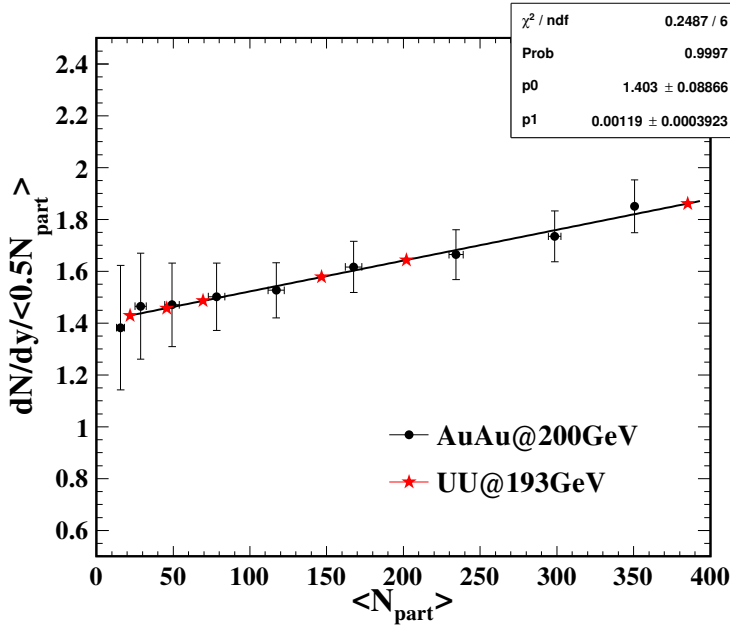


Figure 43: The π^0 yields (black dots) scaled by $N_{part}/2$ as a function of N_{part} is fitted by a first-order polynomial function (black line). The π^0 yields of U + U collisions for different centralities (red stars) are evaluated by this fit function.

Table 5: The scale factors (R_{π^0}) for different centralities in U + U collisions at 193 GeV, with respect to the dN_{π^0}/dy (98.49) Au + Au minimum-bias collisions at 200 GeV.

Centrality (%)	dN_{π^0}/dy	R_{π^0}	$\langle N_{coll} \rangle$
0-80	115.76	1.175	350.08
60-80	15.72	0.160	22.48
40-80	33.35	0.339	63.05
40-60	51.65	0.524	103.61
10-40	165.90	1.684	467.44
0-10	358.48	3.640	1146.12

⁴⁹⁹ (two-body decay or Dalitz decay). The electron pair mass of two-body decay
⁵⁰⁰ follows a narrow Breit-Wigner distribution as given in Eq. 8

$$\frac{dN}{dM_{ee}} = \frac{2\Gamma_0}{(M_{ee} - M_h)^2 + \Gamma_0^2/4} \quad (8)$$

⁵⁰¹ where the Γ_0 represents the PDG [12] width, and M_h is the mass of the hadron
⁵⁰² which decays into the dielectron. The electron pair mass (M_{ee}) is constrained
⁵⁰³ to $[2m_e, 4 \text{ GeV}/c^2]$, where the m_e is the electron mass. The electron pair mass
⁵⁰⁴ of Dalitz decay follows the Kroll-Wada formula [13] as given in Eq. 9,

$$\frac{dN}{dM_{ee}} = PS \cdot |F(M_{ee}^2)|^2 \cdot QED \quad (9)$$

⁵⁰⁵ Where PS is the phase space term defined in Eq. 10. The M_h is mass of the
⁵⁰⁶ hadron which undergoes a Dalitz decay process ($h \rightarrow X e^+ e^-$) and X is the
⁵⁰⁷ third daughter particle with a mass M_X . if X is massless (e.g. γ in π^0, η, η'
⁵⁰⁸ Dalitz decay), the phase space term simplifies to Eq. 11.

$$PS = \left(\left(1 + \frac{M_{ee}^2}{M_h^2 - M_X^2} \right)^2 - \frac{4M_h^2 M_{ee}^2}{(M_h^2 - M_X^2)^2} \right)^{\frac{3}{2}} \quad (10)$$

$$PS = \left(1 - \frac{M_{ee}^2}{M_h^2} \right)^3 \quad (11)$$

⁵¹⁰ The QED term is described by Eq. 12, where N represents a degeneracy
⁵¹¹ factor that depends on how many photons can convert. N is 4 for ω and ϕ
⁵¹² while it is 2 for other hadrons undergoing Dalitz decay process, involved in
⁵¹³ this analysis. The α is the fine-structure constant ($\sim 1/137$).

$$QED = \frac{N \cdot \alpha}{3\pi} \sqrt{1 - \frac{4m_e^2}{M_{ee}^2}} \left(1 + \frac{2m_e^2}{M_{ee}^2} \right) \frac{1}{M_{ee}} \quad (12)$$

⁵¹⁴ The $|F(M_{ee}^2)|^2$ is the electromagnetic form factor. The form factor, described
⁵¹⁵ in Eq. 13, is used for almost all Dalitz decay involved in this analysis except
⁵¹⁶ η' .

$$|F(M_{ee}^2)|^2 = \left(\frac{1}{1 - M_{ee}^2 \Lambda^{-2}} \right)^2 \quad (13)$$

where the Λ^{-2} is the form factor slope, listed in Tab. 6. For π^0 the form factor is usually given by Eq. 14,

$$|F(M_{ee}^2)|^2 = (1 + M_{ee}^2 \Lambda^{-2})^2 \quad (14)$$

For η' , the form factor is given by Eq. 15. The Λ^{-2} and Γ_0^2 are from the fit to the data presented in [16], where the Λ^{-2} and Γ_0^2 are 1.8396 and 1.99×10^{-2} , respectively.

$$|F(M_{ee}^2)|^2 = \frac{1}{(1 - M_{ee}^2 \Lambda^{-2})^2 + \Gamma_0^2 \Lambda^{-2}} \quad (15)$$

Table 6: The electromagnetic form factor slope of mesons.

Meson	Λ^{-2}
π^0	1.756 [14]
η	1.95 [15]
η'	1.8396 [16]
ω	2.24 [15]
ϕ	3.8 [17]

The correlated heavy flavor contributions ($c\bar{c}$, $b\bar{b}$, and Drell-Yan) to the cocktail are obtained from the PYTHIA [7] simulation. These three sources are first simulated in $p + p$ collisions and then scaled by N_{coll} , listed in Tab. 5, to account for the contributions in U + U collisions. The parameter settings (other parameters use the STAR default tune) for different heavy flavors in PYTHIA (version 6.419) are listed below:

- (i) $c\bar{c}$: MSEL = 4 (c trigger), PARP(91) = 1 ($\langle k_T \rangle = 1.0 \text{ GeV}/c$), PARP(67) = 1.0 (parton shower level).
- (ii) $b\bar{b}$: MSEL = 5 (b trigger), PARP(91) = 1.5 ($\langle k_T \rangle = 1.5 \text{ GeV}/c$).
- (iii) Drell-Yan: MSEL = 11 (Z_0 or γ^* trigger), PARP(91) = 1.5 ($\langle k_T \rangle = 1.5 \text{ GeV}/c$).

The charm settings are tuned to match the STAR measurement of the charmed-meson spectrum in $p + p$ collisions [18]. The input charm-pair production cross section is also from the STAR measurements [18, 19]. The Drell-Yan setting are tuned to match the theoretical calculation, and the same PYTHIA settings (except trigger setting) are used in the bottom simulation. The input bottom and Drell-Yan production cross sections are $\sigma_{pp}^{b\bar{b}} = 37 \mu\text{b}$, $\sigma_{pp}^{DY} = 42 \text{ nb}$.

All the physics results reported in Chap. 7 are not corrected for the STAR detector resolution. It's very challenging to precisely reproduce the momentum resolution through embedding, due to various distortion effects in the TPC in the high luminosity RHIC environment. However, a data-driven method is involved in the hadronic cocktail simulation, accounting for these effects [2]. In the Run12 U + U minimum-bias embedding, the reconstructed electron p_T^{rec} probability at a given input p_T^{MC} can be described by a double crystal ball function, given in Eq. 16

$$P(p_T^{rec}, p_T^{MC}) \propto \begin{cases} A \times (B - R)^{-n}, & R < -\alpha \\ e^{-\frac{R^2}{2}}, & -\alpha \leq R < \beta \\ C \times (D + R)^{-m}, & R \geq \beta \end{cases} \quad (16)$$

with

$$\begin{aligned} A &= \left(\frac{n}{|\alpha|} \right)^n \times e^{-\frac{\alpha^2}{2}} \\ B &= \frac{n}{|\alpha|} - |\alpha| \\ C &= \left(\frac{m}{|\beta|} \right)^m \times e^{-\frac{\beta^2}{2}} \\ D &= \frac{m}{|\beta|} - |\beta| \\ R &= \left(\frac{p_T^{rec} - p_T^{MC}}{p_T^{MC}} - \mu \right) / \frac{\sigma_{p_T}}{p_T} \end{aligned} \quad (17)$$

where $n = 1.29$, $\alpha = 1.75$, $m = 2.92$, and $\beta = 1.84$ in Run10 and Run11 Au + Au minimum-bias collisions at 200 GeV [2], are employed in this analysis.

551 The $\mu = -0.001$ is slightly shifted from 0, because the energy loss is taken
 552 into account for STAR tracking with an assumption that all tracks are pions.

553 The electron p_T resolution (σ_{p_T}/p_T) as a function of p_T is evaluated from
 554 Run12 U + U embedding, shown in Fig. 44. This distribution can be de-
 555 scribed by Eq. 18,

$$\sigma_{p_T}/p_T = \sqrt{(a \times p_T)^2 + b^2} \quad (18)$$

556 The two parameters of Eq. 18 are tuned to match the J/ψ signal from the
 557 simulation with that from data. These two parameters used in this analysis
 558 are also the same as that used in Run10 and Run11 minimum-bias collisions
 559 at 200 GeV [2], which are $a = 6.0 \times 10^{-3}$ c/GeV and $b = 8.3 \times 10^{-3}$.

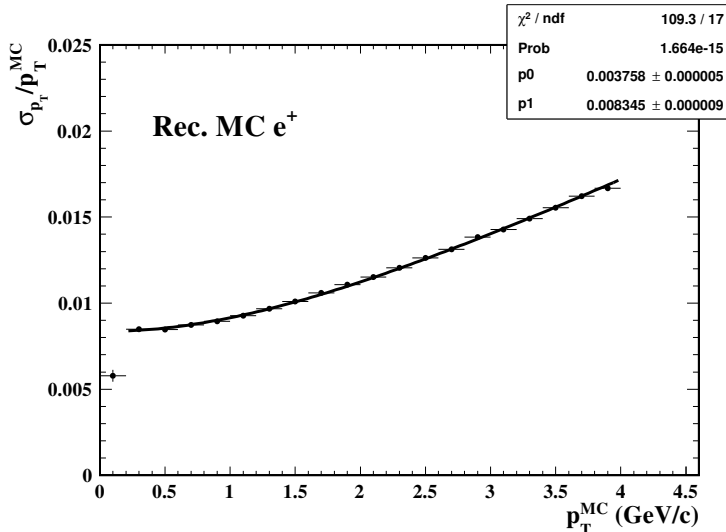


Figure 44: The transverse momentum resolution for positron as a function of p_T from Run12 U + U minimum-bias embedding sample.

560 Figure 45 shows the cocktail simulation within STAR acceptance including
 561 the light hadrons decay and correlated heavy flavor decay in U + U minimum-
 562 bias collisions at 193 GeV. The cocktails of different acceptance settings and
 563 the cocktail within STAR acceptance including the detector efficiency losses
 564 in U + U minimum-bias collisions at 193 GeV are depicted in Fig. 46. As
 565 discussed in Sec. 4.2, the dielectron pair efficiency within STAR acceptance
 566 and STAR acceptance factor can be evaluated from Fig. 46.

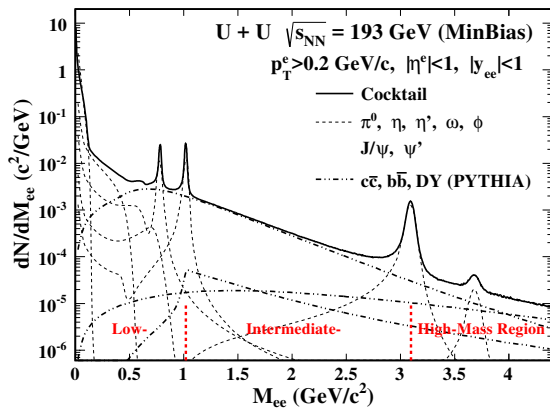


Figure 45: The cocktail simulation within STAR acceptance (solid line) including the light hadrons decay and correlated heavy flavor decay (dashed lines) in $U + U$ minimum-bias collisions at 193 GeV.

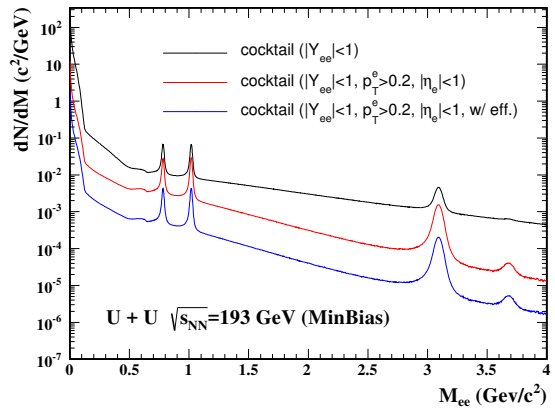


Figure 46: The cocktails of different acceptance settings (Black - before filtering STAR acceptance; Red - within STAR acceptance) and the cocktail within STAR acceptance including the detector efficiency losses (Blue) in $U + U$ minimum-bias collisions at 193 GeV.

567 6 Systematic Uncertainties

568 The sources of the systematic uncertainty that contribute to the final result
 569 in this analysis are listed below:

- 570 (i) Background subtraction.
- 571 (ii) Hadron contamination.
- 572 (iii) Efficiency correction.
- 573 (iv) Cocktail simulation.

574 **Background subtraction** In this analysis, the acceptance corrected like-sign
 575 background is subtracted for obtaining the raw signal. Where the acceptance
 576 factor is calculated by the ratio of the mixed-event unlike-sign and like-
 577 sign distribution. The systematic uncertainty of the acceptance factor can be
 578 evaluated by varying the event categories (varying the number of V_z , central-
 579 ity and event-plane bins) and event-pool size. The difference between 2-D

580 (M_{ee} , p_T^{ee}) and 1-D (M_{ee}) acceptance corrections is also taken into account
581 only for the regular dielectron analysis. For this very low $p_T e^+e^-$ analysis
582 in Au + Au and U + U collisions, the unlike-sign and like-sign acceptance
583 difference correction factor results in 1-8% p_T , mass dependent uncertainty.

584 **Hadron contamination** The identified electron candidates contain a small
585 amount of fast hadrons, as discussed in Sec. 2.3. If these hadrons are cor-
586 related with other particles (e.g. resonance decays), they may contribute
587 into the final signal spectrum. The electron purity and the relative ratios of
588 hadron over electron in the identified electron sample are shown in Fig. 9 and
589 Fig. 47, respectively. To estimate the contribution of the hadron contamina-
590 tion, the pure hadron samples are firstly selected by a tight m^2 cut (shown in
591 Fig. 3). We randomly picked hadrons from these pure samples according to
592 the hadron contamination levels in both total and the p_T differential yields,
593 creating a hadron pool. The same procedure used in the dielectron analysis
594 is applied to the hadron contamination pool to estimate the $e - h$ and $h - h$
595 contribution. The effect in U + U collisions at 193 GeV is similar to that in
596 Au + Au collisions at 200 GeV. According to the published STAR dielectron
597 long paper [2], the relative contribution to the final spectrum at very low p_T
598 is <4%.

599 **Efficiency correction** The systematic uncertainty caused by efficiency correc-
600 tion includes uncertainties on the single track efficiency which is folded into
601 the pair efficiency, the pair efficiency evaluated by different methods and the
602 ϕ_V cut efficiency. The systematic uncertainty on TPC tracking efficiency
603 (nHitsFit, dca) is evaluated by varying the selection cuts in the data and MC
604 embedding at the same time and then comparing the difference between the
605 change of data and MC embedding. The systematic uncertainties on nHits-
606 Dedx cut, $n\sigma_e$ cut and the TOF matching are evaluated by comparing the
607 corresponding efficiency differences between different pure electron samples

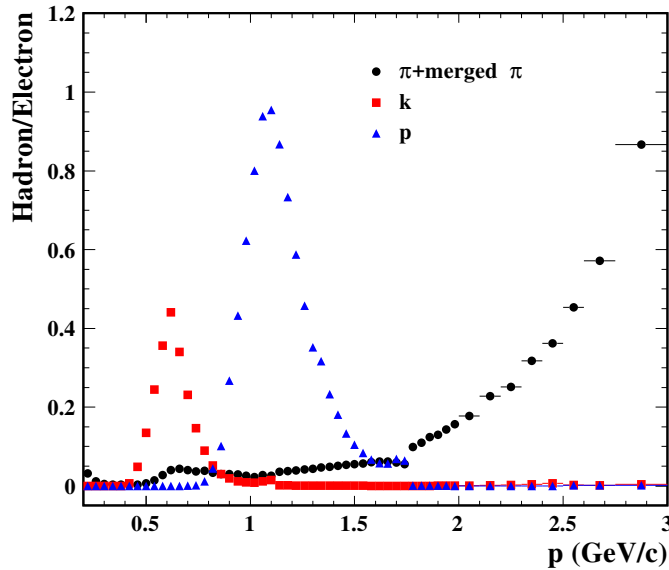


Figure 47: The relative ratio of hadrons over electrons in the identified electron sample as a function of momentum in $U + U$ minimum-bias collisions at 193 GeV.

(using different invariant mass cuts to select the pure electron samples). The systematic uncertainty on the $1/\beta$ cut efficiency is evaluated by comparing the efficiency difference between direct bin counting method and Gaussian fit (discussed in Sec. 4.1.4). These systematic uncertainties owing to the single track efficiency are summarized in Tab. 7. Due to the unknown heavy flavor correlation in the medium, two extreme methods (discussed in Sec. 4.2) are employed to fold the single track efficiency into the pair efficiency. The difference of the pair efficiency between these two methods are also taken into account for the efficiency correction systematic uncertainty. Combining all the aforementioned components, the uncertainties on the detector efficiency correction are $\sim 13\%$ (see details in p19-p20 of Ref. [2]) and $\sim 11\%$ in $Au + Au$ and $U + U$ collisions, respectively. The systematic uncertainty of the ϕ_V cut efficiency, only considered in regular dielectron analysis, is evaluated by comparing the difference between the efficiency from the π^0 embedding sample and the virtual photon decay sample.

623 **Cocktail simulation** The systematic uncertainty of the cocktail simulation
624 is evaluated by folding the systematic uncertainties of meson yields and the
625 heavy flavor cross sections.

626 The total systematic uncertainty is determined via the quadratic sum of
627 the contribution of each component.

Table 7: Systematic uncertainties on single track efficiency.

	Component	Uncertainty (%)
TPC	nHitsFit	3.4
	DCA	1.8
	nHitsdEdx	1.1
TOF	$n\sigma_e$	0.5
	Matching	1.4
	$1/\beta$	2.4
	Total	4.9

628 7 Physics Results

629 7.1 Consistency Check Between Run10 and Run11 Au + Au Col- 630 lisions

631 For the Au + Au minimum-bias triggered data, the efficiency corrected
632 spectra are obtained separately for run 2010 and run 2011, and then combined
633 point by point according to their relative statistical uncertainties. Before
634 combining the results, consistency check between these two runs has been
635 done, which are shown in Figs. 48, 49, 50, 51, and 52.

636 7.2 Low p_T e^+e^- Paper Plots

637 To measure the true other than fiducial excess yields, the detector accep-
638 tance ($p_T^e \geq 0.2 \text{ GeV}/c, |\eta_e| \leq 1, |Y_{ee}| \leq 1$) should be corrected for. The
639 acceptance factor is estimated as the yield ratio of reconstructed e^+e^- pairs

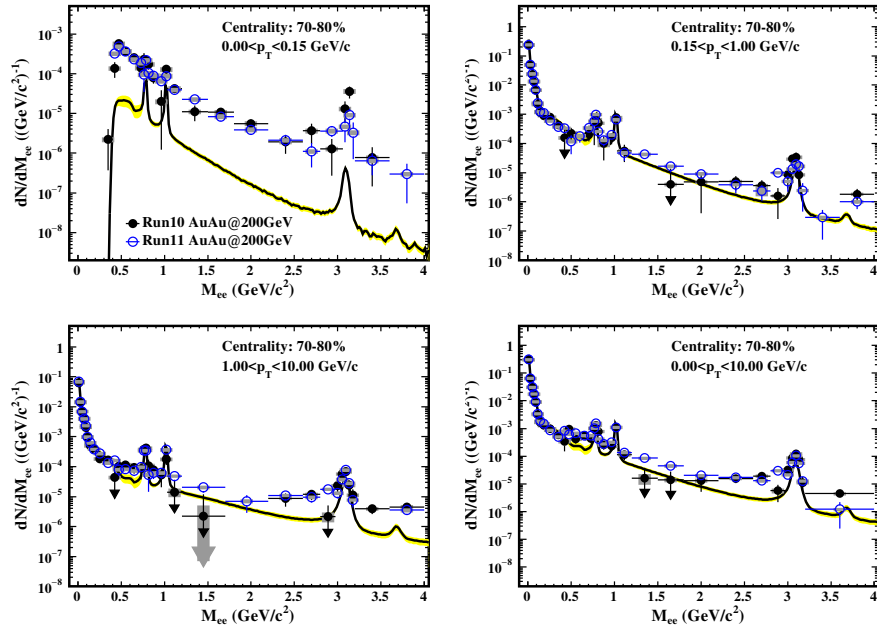


Figure 48: The efficiency-corrected mass spectra within STAR acceptance from 70-80% central Run10 and Run11 Au + Au collisions in various p_T bins.

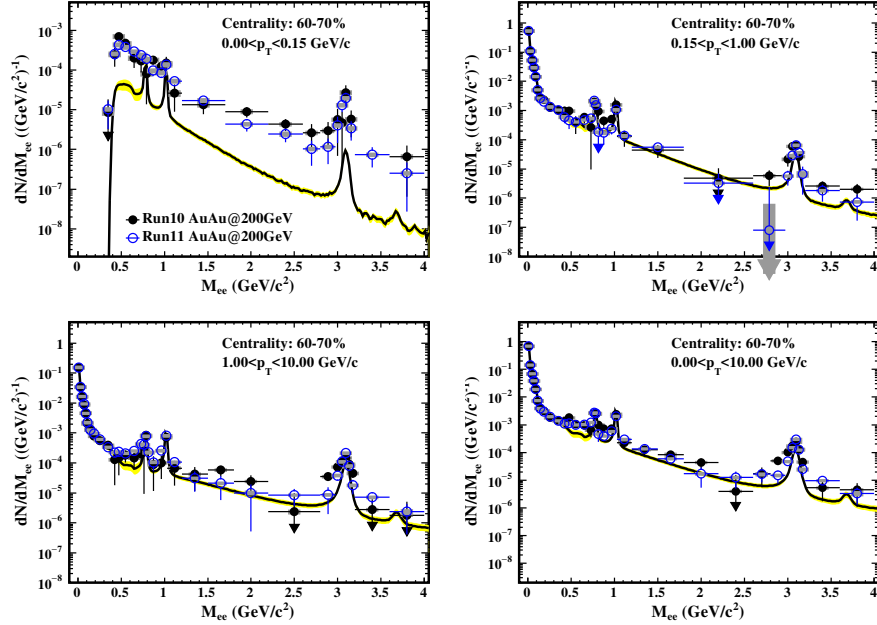


Figure 49: The efficiency-corrected mass spectra within STAR acceptance from 60-70% central Run10 and Run11 Au + Au collisions in various p_T bins.

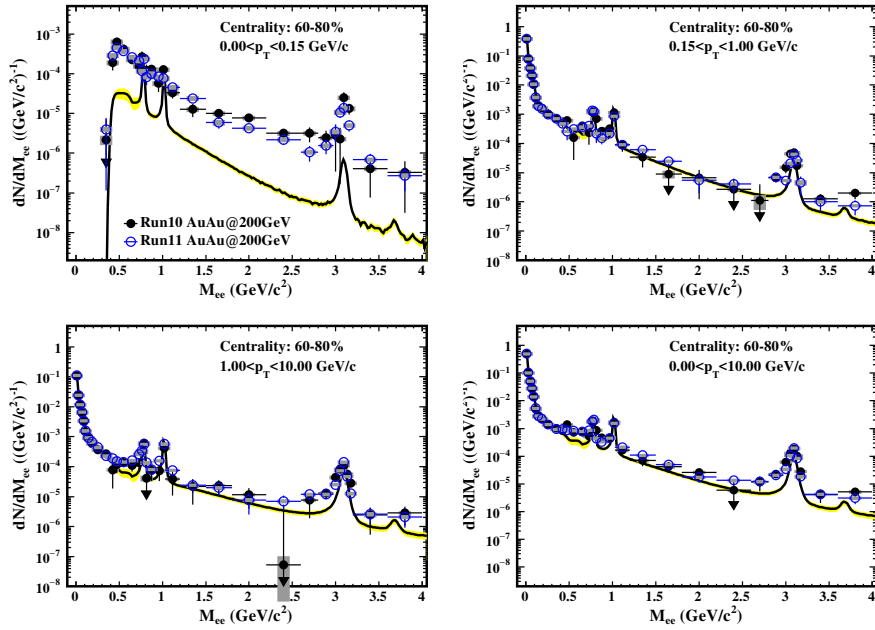


Figure 50: The efficiency-corrected mass spectra within STAR acceptance from 60-80% central Run10 and Run11 Au + Au collisions in various p_T bins.

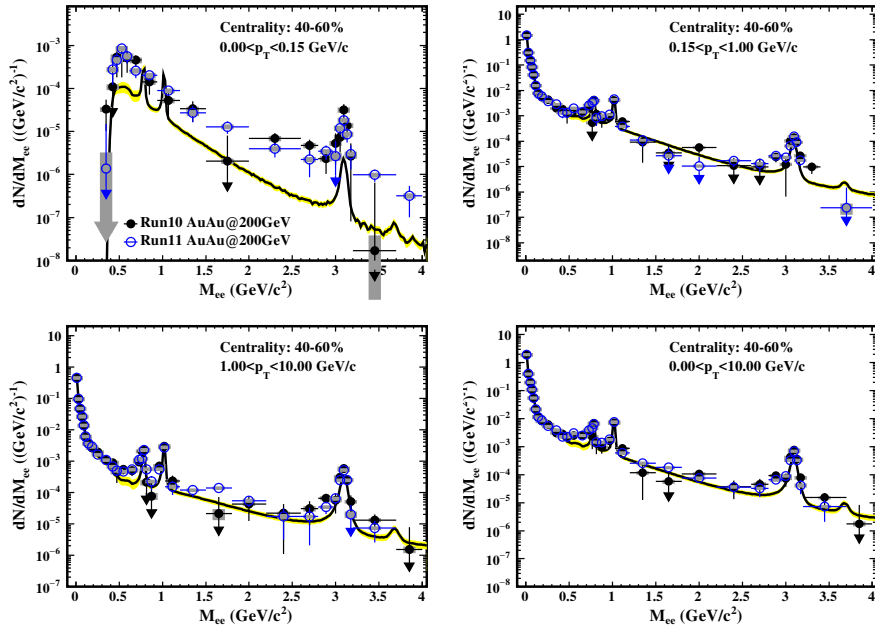


Figure 51: The efficiency-corrected mass spectra within STAR acceptance from 40-60% central Run10 and Run11 Au + Au collisions in various p_T bins.

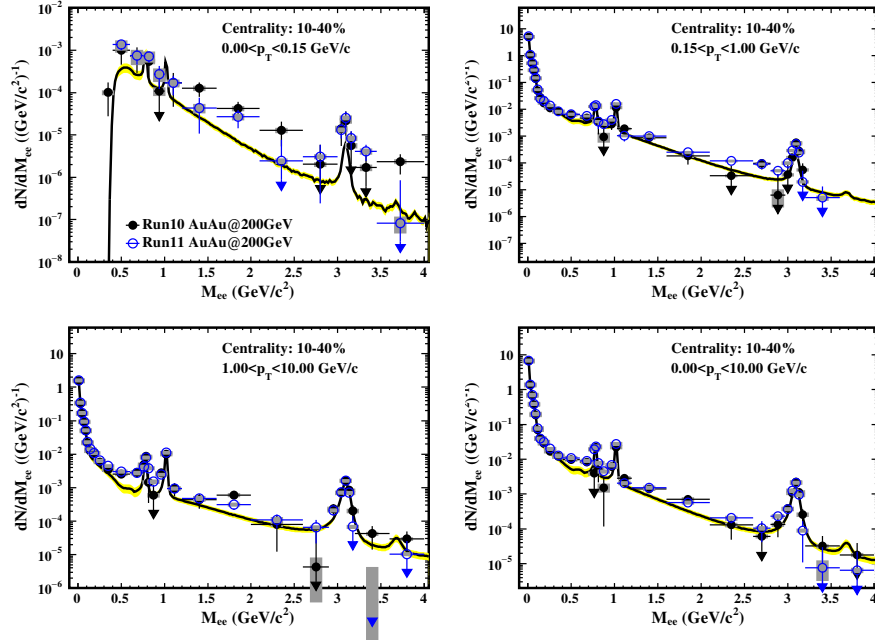


Figure 52: The efficiency-corrected mass spectra within STAR acceptance from 10-40% central Run10 and Run11 Au + Au collisions in various p_T bins.

Table 8: The χ^2/NDF values of all the fittings in Fig. 56. The “w/o” stands for without STAR acceptance corrected for while “w/” stands for with STAR acceptance corrected for.

Mass (GeV/c^2)	Au + Au w/o (w/)	U + U w/o (w/)
0.4-0.76	2.46/4 (1.47/4)	0.92/2 (1.16/2)
0.76-1.2	0.99/3 (1.10/3)	0.79/2 (0.82/2)
1.2-2.6	0.31/2 (0.55/2)	0.34/3 (0.45/3)

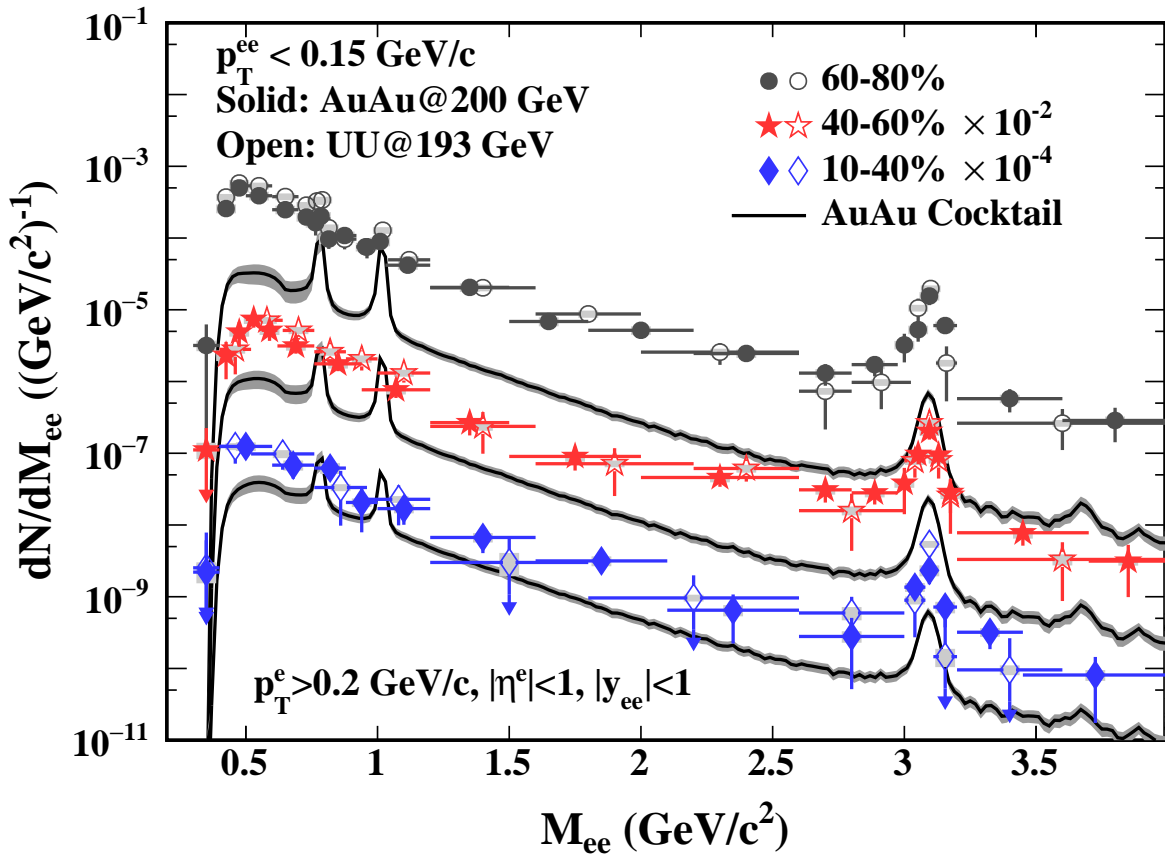


Figure 53: Centrality dependence of e^+e^- invariant mass spectrum within the STAR acceptance ($p_T^e > 0.2 \text{ GeV}/c$, $|\eta^e| < 1$, and $|y_{ee}| < 1$) from Au + Au collisions (solid markers) and U + U collisions (open markers) for e^+e^- pair $p_T < 0.15 \text{ GeV}/c$. The mass spectra are compared to hadronic cocktail simulations shown as solid lines. The hadronic cocktails from U + U collisions are slightly higher than those from Au + Au collisions for given centrality bins. Only Au + Au cocktails are shown in this figure for clarity. The vertical bars on data points depict the statistical uncertainties, while the systematic uncertainties are shown as grey boxes. The shaded bands on the solid lines depict the systematic uncertainties on the cocktail.

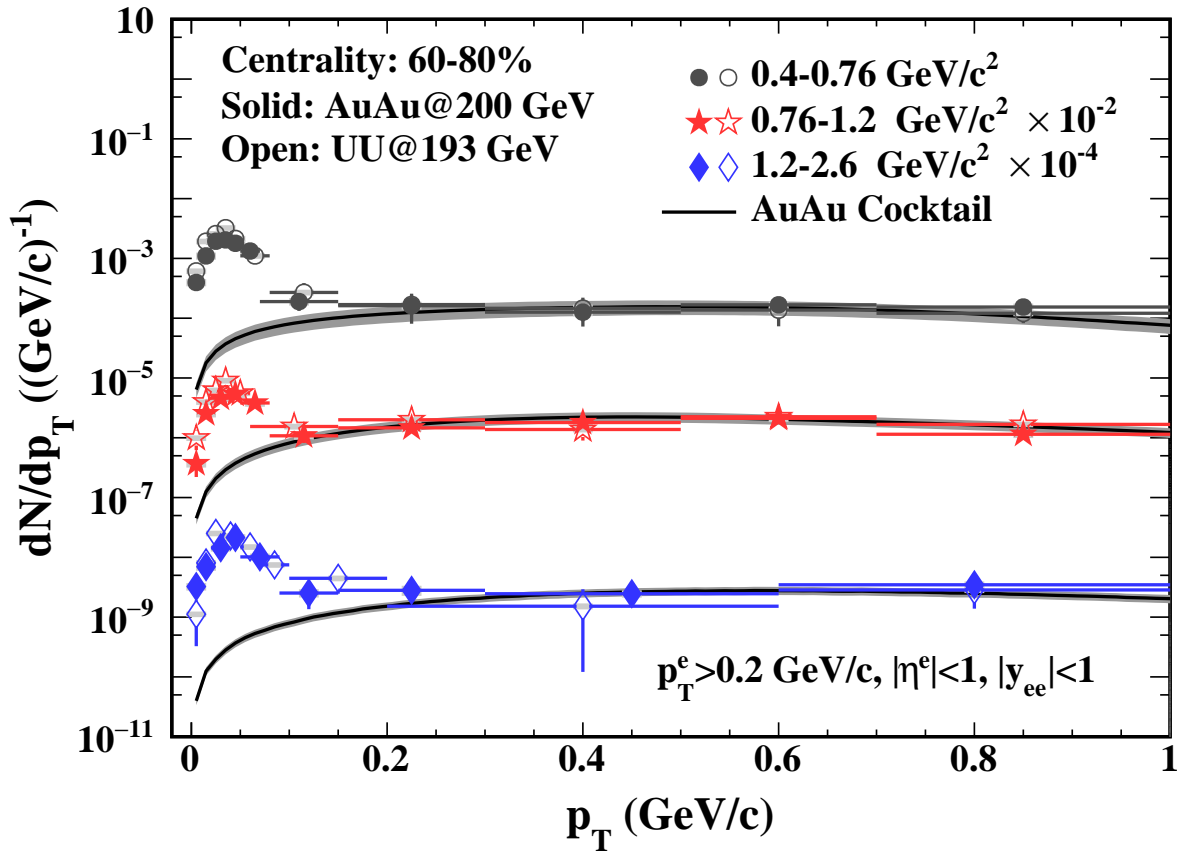


Figure 54: The e^+e^- pair p_T distributions within STAR acceptance for different mass regions in 60-80% Au+Au (solid markers) and U+U (open markers) collisions compared to cocktail simulations (solid curves). The systematic uncertainties of the data are shown as gray boxes. The brown bands depict the systematic uncertainties of the cocktail simulations.

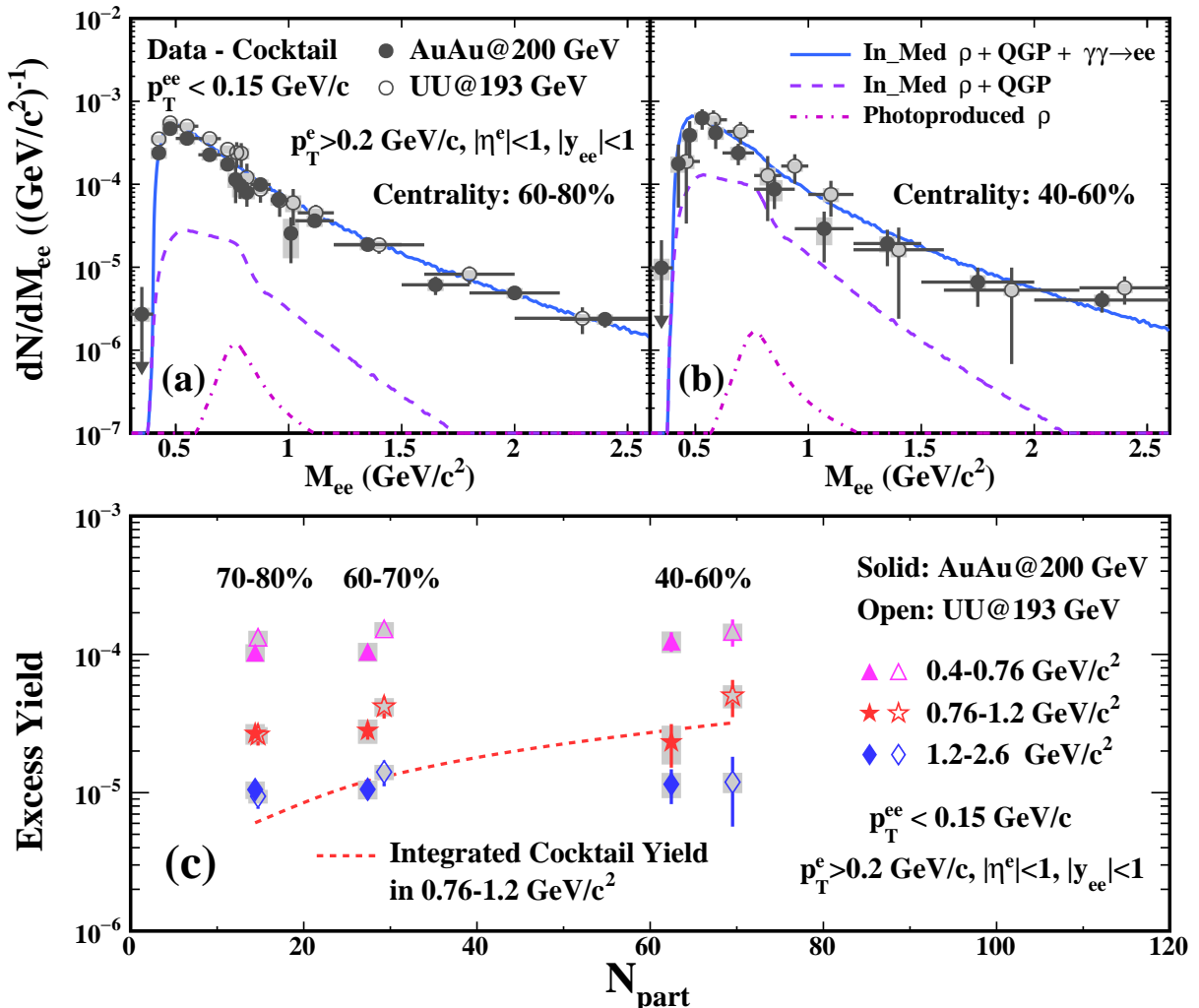


Figure 55: The low p_T ($p_T < 0.15 \text{ GeV}/c$) e^+e^- excess mass spectra (data-cocktail) within STAR acceptance in 60-80% (a), 40-60% (b) Au+Au (solid dots) and U+U (open circles) collisions, compared with a broadened ρ model calculation. The contributions of ρ from the photonuclear process and from the photon-photon process are also shown. Panel (c) shows the centrality dependence of integrated excess yields in the mass regions of 0.4-0.76, 0.76-1.2, and 1.2-2.6 GeV/c 2 in Au + Au (solid markers) and U + U (open markers) collisions. The centrality dependence of hadronic cocktail yields in the mass region of 0.76-1.2 GeV/c 2 is also shown for comparison. The systematic uncertainties of the data are shown as gray boxes.

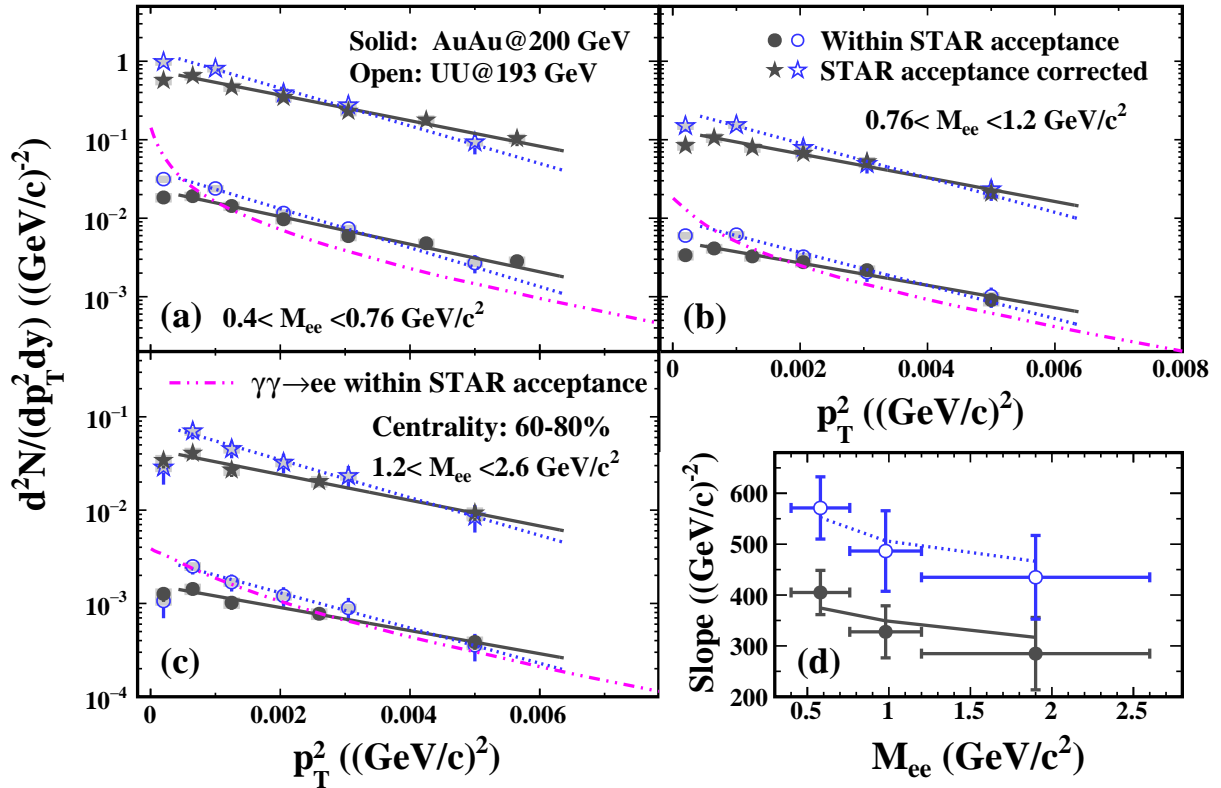


Figure 56: The p_T^2 distributions of excess yields within STAR acceptance (solid and open circles) and with STAR acceptance corrected for (solid and open stars) in the mass regions of 0.4 - 0.76 (a), 0.76 - 1.2 (b), and 1.2 - 2.6 (c) GeV/c^2 in $60- 80% Au+Au (solid markers) and U+U (open markers) collisions. The systematic uncertainties of the data are shown as gray boxes. The solid and dotted lines are exponential fits to the data in Au+Au and U+U collisions, respectively. The χ^2/NDF values of the fits are summarized in Tab. 8. The dash-dotted lines represent the p_T^2 distributions from photon-photon process within STAR acceptance in $60- 80% Au+Au collisions. Panel (d): The corresponding slope parameters of p_T^2 distributions within STAR acceptance (solid and open circles) and with STAR acceptance corrected for (lines) in Au+Au (solid) and U+U (open) collisions.$$

in the STAR detector over the input e^+e^- pairs with $|y_{ee}| < 1$, as shown in the following equation:

$$\varepsilon_{Acc} = \frac{dN/dM_{ee} (p_T^e \geq 0.2 \text{ GeV}/c, |\eta_e| \leq 1, |Y_{ee}| \leq 1)}{dN/dM_{ee} (|Y_{ee}| \leq 1)} \quad (19)$$

The acceptance correction factor highly depends on the underlying physics mechanisms, for instance, the correction factor could vary by a factor of 10 between hadronic two-body decay and two-photon interaction processes (see p11 in http://www.star.bnl.gov/protected/lfsupc/syang/dielectronPaper/lowPtWebPage/SupportingDoc/20171108_Efficiency_CrossCheck_VPvsGammaGamma.pdf). From the physics results in Figs. 53, 54, 55, the observed excess is very likely to be linked to the photon-photon interaction. Under this assumption, the acceptance correction is evaluated via the same model calculation of photon-photon interaction depicted in Fig. 55. The details of the two-photon model calculation can be found in Sec. 7.3. The calculations fall below data points at large p_T^2 values while overshoot data at low p_T^2 , especially at extremely low p_T region. The discrepancy could be partially attributed to the fact that only real photons and lowest-order QED are considered in the Equivalent Photon Approximation (EPA) approach. Thus, the pair p_T distributions in the two-photon model calculations are modified to match the measured data for the acceptance correction factor evaluations. The systematic uncertainty on the acceptance correction is estimated by varying the pair p_T distribution, resulting in $\sim 2\%$ uncertainties for $0 < p_T^2 < 0.0064 \text{ (GeV}/c)^2$ in three mass differentials. The acceptance factors as a function of p_T^2 are shown in Fig. 57, while the ratios of acceptance correction factors with different p_T distribution inputs are shown in Fig. 58.

7.3 The model calculation of photon-photon interaction in peripheral Au + Au collisions (done by Wangmei Zha)

The content of this section is directly copied from Wangmei's paper draft of "Coherent lepton pair production in hadronic heavy

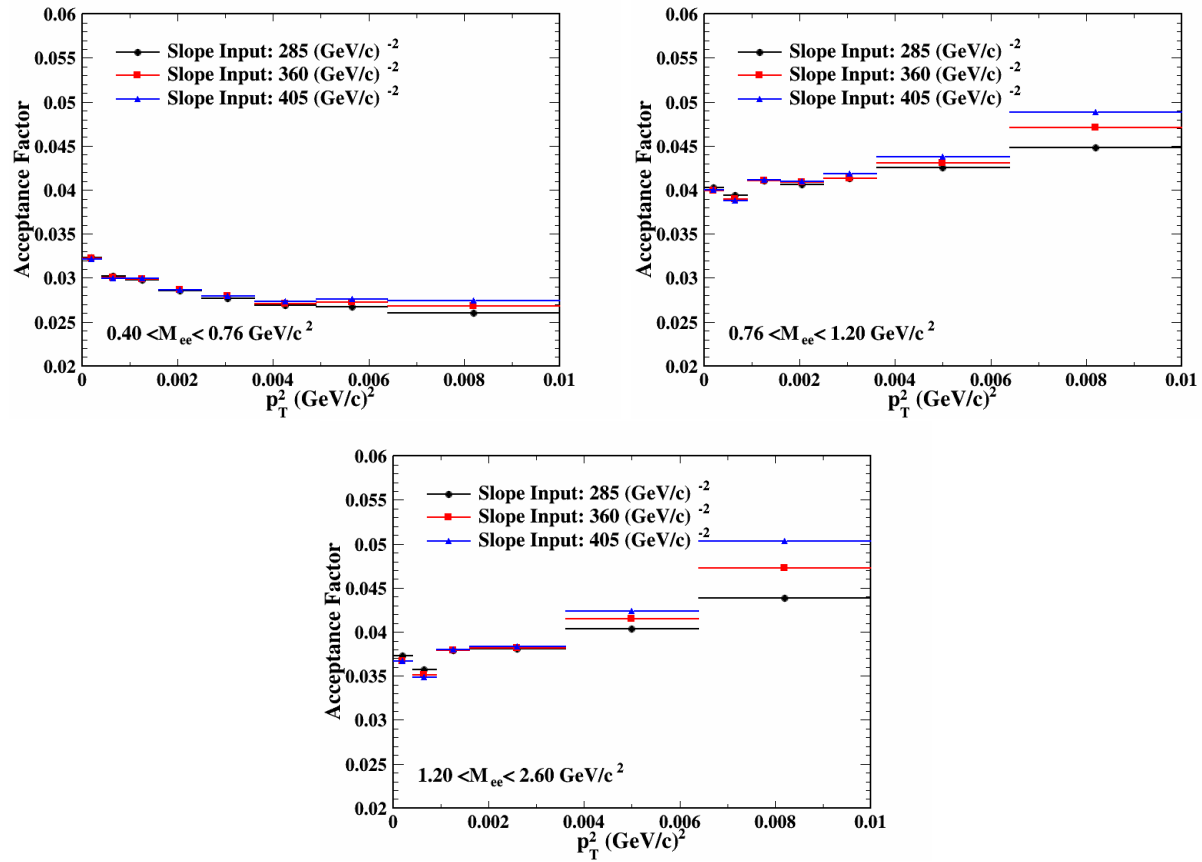


Figure 57: The detector acceptance correction factors derived by the “ $\gamma\gamma \rightarrow e^+e^-$ ” calculations with different pair p_T distributions.

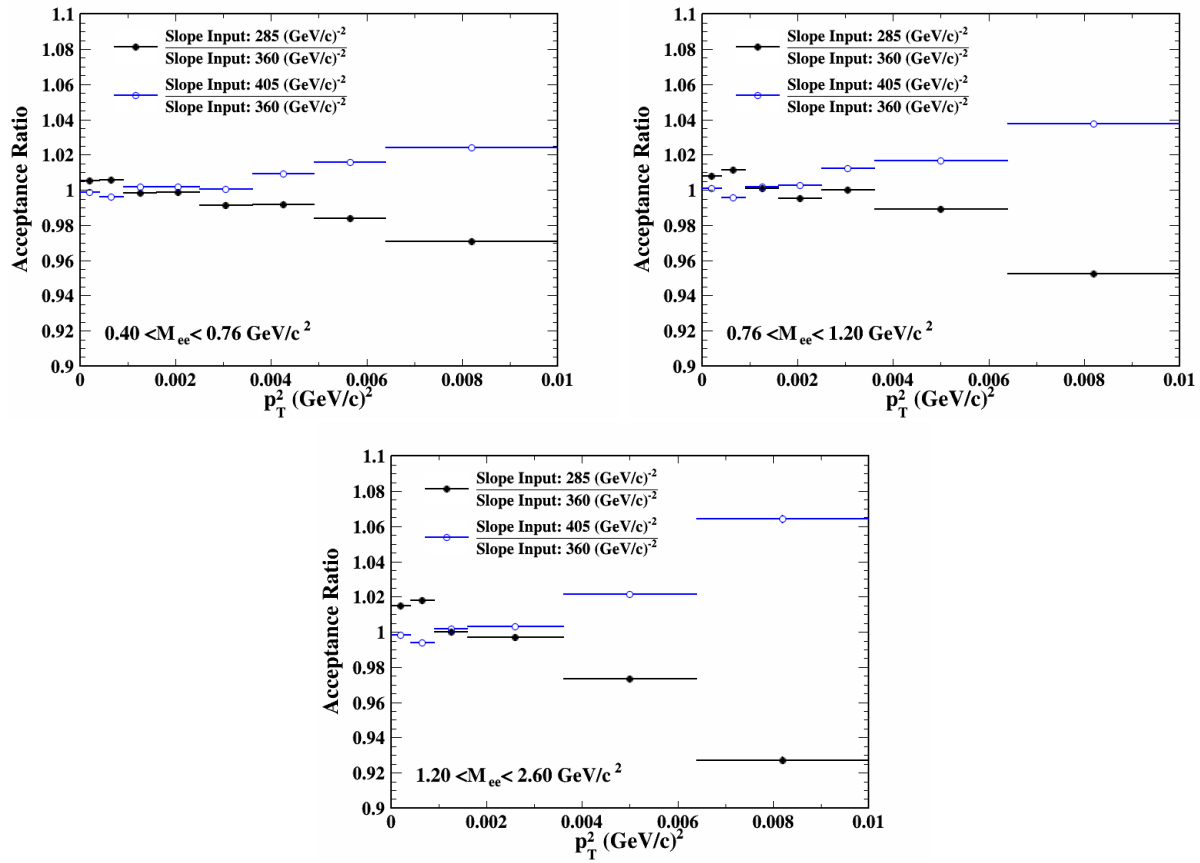


Figure 58: The acceptance correction factor ratios as a function of p_T^2 in three mass differentials.

⁶⁶⁷ **ion collisions". This theoretical model calculation paper is in prepa-**
⁶⁶⁸ **ration, but is expected to be released before the STAR very low p_T**
⁶⁶⁹ **e^+e^- paper.**

⁶⁷⁰ According to the equivalent photon approximation method, a two-photon
⁶⁷¹ reaction can be factorized into a semiclassical part and a quantum part. The
⁶⁷² semiclassical part deals with distribution of massless photons swarming about
⁶⁷³ the colliding ions, while the quantum part usually involves the description
⁶⁷⁴ of the interaction between the two emitted photons. The cross section to
⁶⁷⁵ produce a lepton pair with pair mass W can be written as [20]:

$$\begin{aligned} & \sigma(A + A \rightarrow A + A + l^+l^-) \\ &= \int dk_1 dk_2 \frac{n(k_1)}{k_1} \frac{n(k_2)}{k_2} \sigma[\gamma\gamma \rightarrow l^+l^-(W)], \end{aligned} \quad (20)$$

⁶⁷⁶ where k_1 and k_2 are the two photon energies and $n(k)$ is the photon flux at
⁶⁷⁷ energy k . The two photon energies k_1 and k_2 determine the pair mass W and
⁶⁷⁸ rapidity y :

$$k_{1,2} = \frac{W}{2} e^{\pm y} \quad (21)$$

⁶⁷⁹ and

$$y = \frac{1}{2} \ln \frac{k_1}{k_2}. \quad (22)$$

⁶⁸⁰ The photon flux induced by nucleus can be modelled using the Weizsäcker-
⁶⁸¹ Williams method [21]. For the point-like charge distribution, the photon flux
⁶⁸² is given by the simple formula

$$n(k, r) = \frac{d^3 N}{dk d^2 r} = \frac{Z^2 \alpha}{\pi^2 k r^2} x^2 K_1^2(x) \quad (23)$$

⁶⁸³ where $n(k, r)$ is the flux of photons with energy k at distant r from the center
⁶⁸⁴ of nucleus, α is the electromagnetic coupling constant, $x = kr/\gamma$, and γ is
⁶⁸⁵ lorentz factor. Here, K_1 is a modified Bessel function. For realistic case, the
⁶⁸⁶ charge distribution in nucleus should be take into account for the estimation
⁶⁸⁷ of photon flux. A generic formula for any charge distribution can be written

as:

$$n(k, r) = \frac{4Z^2\alpha}{k} \left| \int \frac{d^2 q_\perp}{(2\pi)^2} q_\perp \frac{F(q)}{q^2} e^{iq_\perp \cdot r} \right|^2 \quad (24)$$

$$q = (q_\perp, \frac{k}{\gamma})$$

where the form factor $F(q)$ is Fourier transform of the charge distribution in nucleus. In our calculations, we use two-parameter Fermi distribution (called equivalently Woods-Saxon distribution) for charge distribution in nucleus

$$\rho_A(r) = \frac{\rho^0}{1 + \exp[(r - R_{WS})/d]} \quad (25)$$

where the radius R_{WS} and skin depth d are based on fits to electron scattering data [22], and ρ^0 is the normalization factor.

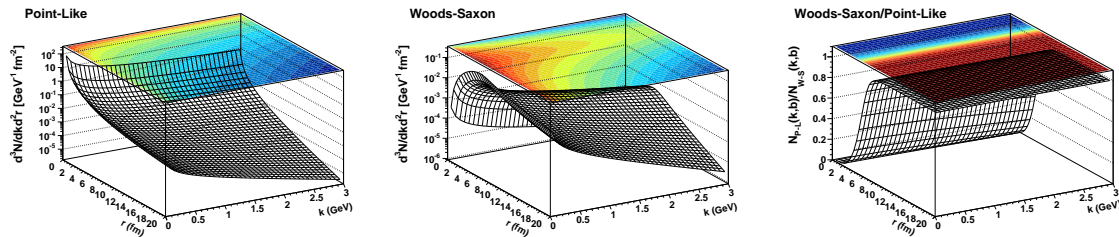


Figure 59: Two-dimensional distributions of the photon flux in the distant r and in the energy of photon k for point-like (left panel) and Woods-Saxon (middle panel) form factors in Au+Au collisions at $\sqrt{s_{NN}} = 200$ GeV. The right panel shows the ratio of the differential photon fluxes with Wood-Saxon form factor to those with point-like form factor.

Figure 59 shows the two-dimensional distributions of the photon flux induced by Au+Au collisions at $\sqrt{s_{NN}} = 200$ GeV as a function of distant r and energy k for point-like (left panel) and Woods-Saxon (middle panel) form factors. The right panel of Fig. 59 shows the ratio of the differential photon fluxes with Wood-Saxon form factor to those with point-like form factor. One can observe that the difference between photon fluxes obtained with point-like form factor and the result for Woods-Saxon photon source is huge inside the nucleus ($r < R_{WS}$). For $r \gg R_{WS}$, the difference is negligible. In this calculation, for $r < 10$ fm, we use the photon flux calculated

⁷⁰³ with Woods-Saxon form factor; while at $r > 10$ fm, the result with point-like
⁷⁰⁴ assumption is employed.

⁷⁰⁵ The elementary cross-section to produce a pair of leptons with lepton
⁷⁰⁶ mass m and pair invariant mass W can be determined by the Breit-Wheeler
⁷⁰⁷ formula [23]

$$\begin{aligned} \sigma(\gamma\gamma \rightarrow l^+l^-) = & \\ \frac{4\pi\alpha^2}{W^2} & [(2 + \frac{8m^2}{W^2} - \frac{16m^4}{W^4}) \ln(\frac{W + \sqrt{W^2 - 4m^2}}{2m}) \\ & - \sqrt{1 - \frac{4m^2}{W^2}}(1 + \frac{4m^2}{W^2})]. \end{aligned} \quad (26)$$

⁷⁰⁸ The angular distribution of these lepton pairs is given by

$$G(\theta) = 2 + 4(1 - \frac{4m^2}{W^2}) \frac{(1 - \frac{4m^2}{W^2}) \sin^2(\theta) \cos^2(\theta) + \frac{4m^2}{W^2}}{(1 - (1 - \frac{4m^2}{W^2}) \cos^2(\theta))^2}, \quad (27)$$

⁷⁰⁹ where θ is the angle between the beam direction and one of the leptons in the
⁷¹⁰ lepton-lepton center of mass frame. Here, we neglect the effect of the photon
⁷¹¹ p_T on the angular distribution.

⁷¹² The approach used in this calculation is very similar to that of the STARlight
⁷¹³ Monte Carlo [20], which is popular for UPCs. STARlight has been extensively
⁷¹⁴ compared with UPC data, with good agreement found for $\gamma + \gamma \rightarrow l^+ + l^-$,
⁷¹⁵ with data from STAR [24], ATLAS [25], ALICE [26] and CMS [?] collab-
⁷¹⁶ oration. In STARlight, a point-like charge distribution for photon flux is
⁷¹⁷ employed and the production for transverse positions within the nucleus is
⁷¹⁸ neglected. This approximation is proper for UPCs, because the production
⁷¹⁹ inside the nucleus is small. However, comes to the hadronic heavy-ion colli-
⁷²⁰ sion, when the two colliding nuclei are very close to each other, the charge
⁷²¹ distribution and the production inside the nucleus can not be neglected. In
⁷²² this calculation, we employ the Woods-Saxon charge distribution, and include
⁷²³ the production inside the nucleus.

⁷²⁴ With the convolution of equivalent photon spectra and elementary cross-
⁷²⁵ section, the probability to produce a lepton pair with pair mass W and rapid-

⁷²⁶ ity y for a collision at impact parameter b can be given by:

$$P(W, y, b) = \frac{W}{2} \int d^2r_1 n(k_1, r_1) n(k_2, |\vec{b} - \vec{r}_1|) \sigma_{\gamma\gamma}(W). \quad (28)$$

⁷²⁷ The invariant yield for coherent lepton pair production in a selected centrality
⁷²⁸ class can be written as:

$$\frac{d^2N}{dWdy} = \frac{\int_{b_{min}}^{b_{max}} d^2b P(W, y, b) \times P_H(\vec{b})}{\int_{b_{min}}^{b_{max}} d^2b P_H(\vec{b})}, \quad (29)$$

⁷²⁹ with the hadronic interaction probability

$$P_H(\vec{b}) = 1 - \exp[-\sigma_{NN} \int d^2r T_A(\vec{r}) T_A(\vec{r} - \vec{b})] \quad (30)$$

⁷³⁰ where σ_{NN} is the inelastic hadronic interaction cross section, $T_A(\vec{r})$ is the
⁷³¹ nuclear thickness function defined as

$$T_A(\vec{r}) = \int dz \rho(\vec{r}, z) dz. \quad (31)$$

⁷³² The b_{min} and b_{max} in Eq. 29 are the minimum and maximum impact pa-
⁷³³ rameters for a given centrality bin, and can be determined from the Glauber
⁷³⁴ Monte Carlo simulations [27]. In hadronic heavy-ion collisions, the coher-
⁷³⁵ ent lepton pair production is accompanied by violent hadronic interactions
⁷³⁶ occurred in the overlap region, which may impose impact on the coherent
⁷³⁷ production. The possible disruptive effects can be considered into two part:
⁷³⁸ photon emission and production in the overlap region. For photon emission,
⁷³⁹ the photon field travels along with the colliding nucleus and they are likely to
⁷⁴⁰ be emitted before the hadronic interactions occur by about $\Delta t \sim r/c$, where r
⁷⁴¹ is the distant from the nucleus. The energetic hadronic collisions in the over-
⁷⁴² lap region happen at a small time scale $t_{coll} \sim R_{WS}/\gamma$. Therefore, the photon
⁷⁴³ emission should be unaffected by hadronic interactions. For the coherent
⁷⁴⁴ production in the overlap region, the product may be affected by the violent
⁷⁴⁵ interactions, leading to the destruction of coherent production. Because the
⁷⁴⁶ final product is lepton pair, which is not subject to the strong interactions in

⁷⁴⁷ the overlap region, the destruction effect should be small. In this calculations,
⁷⁴⁸ we neglect the possible disruption from hadronic interactions. This is appro-
⁷⁴⁹ priate for peripheral collisions, however, it may overestimate the production
⁷⁵⁰ in central collisions.

751 References

- 752 [1] M.L. Miller *et al.*, “Glauber Modeling in High-Energy Nuclear Collisions.”
753 *Annu. Rev. Nucl. Part. Sci.* **57**, 205 (2007).
- 754 [2] L. Adamczyk *et al.* (STAR Collaboration), “Measurements of Dielectron
755 Production in Au+Au Collisions at $\sqrt{s_{NN}} = 200$ GeV from the STAR
756 Experiment.” *Phys. Rev. C* **92**, 24912 (2015).
- 757 [3] A. Adare *et al.* (PHENIX Collaboration), “Detailed measurement of the
758 e^+e^- pair continuum in $p + p$ and Au + Au collisions at $\sqrt{s_{NN}} = 200$
759 GeV and implications for direct photon production.” *Phys. Rev. C* **81**,
760 034911 (2010).
- 761 [4] A. M. Poskanzer and S. A. Voloshin, “Methods for analyzing anisotropic
762 flow in relativistic nuclear collisions.” *Phys. Rev. C* **58**, 1671 (1998).
- 763 [5] J. Adams *et al.* (STAR Collaboration), “Azimuthal anisotropy in Au +
764 Au collisions at $\sqrt{s_{NN}} = 200$ GeV.” *Phys. Rev. C* **72**, 014904 (2005).
- 765 [6] CERN Program Library Long Write-up W5013,
766 “GEANT - Detector Simulation and Simulation Tool”
767 http://wwwwasdoc.web.cern.ch/wwwwasdoc/geant_html3/geantall.html.
- 768 [7] Torbjörn Sjöstrand *et al.*, “High-energy-physics event generation with
769 Pythia 6.1.” *Comput. Phys. Commun.* **135**, 238 (2001).
- 770 [8] D. Kikola *et al.*, “Prospects for quarkonia production studies in U + U
771 collisions.” *Phys. Rev. C* **84**, 054907 (2011).
- 772 [9] Z. B. Tang *et al.*, “Spectra and radial flow in relativistic heavy ion col-
773 lisions with Tsallis statistics in a blast-wave description.” *Phys. Rev. C*
774 **79**, 051901 (2009).
- 775 [10] Z. B. Tang *et al.*, “The Statistical Origin of Constituent-Quark Scaling
776 in QGP Hadronization.” *Chin. Phys. Lett.* **30**, 031201 (2013).

- [11] B. I. Abelev *et al.* (STAR Collaboration), “Systematic measurements of identified particle spectra in pp , $d + \text{Au}$, and $\text{Au} + \text{Au}$ collisions at the STAR detector.” *Phys. Rev. C* **79**, 034909 (2009).
- [12] K. A. Olive *et al.* (Particle Data Group), “REVIEW OF PARTICLE PHYSICS.” *Chin. Phys. C* **38**, 090001 (2014).
- [13] N. M. Kroll, W. Wada, “Internal Pair Production Associated with the Emission of High-Energy Gamma Rays.” *Phys. Rev.* **98**, 1355 (1955).
- [14] K Nakamura *et al.*, “Review of Particle Physics.” *J. Phys. G* **37**, 075021 (2010).
- [15] R. Arnaldi *et al.* (NA60 Collaboration), “Study of the electromagnetic transition form-factors in $\eta \rightarrow \mu^+ \mu^- \text{gamma}$ and $\omega \rightarrow \mu^+ \mu^- \pi^0$ decays with NA60.” *Phys. Lett. B* **677**, 260 (2009).
- [16] L.G. Landsberg, “Electromagnetic decays of light mesons.” *Phys. Rept.* **128**, 301 (1985).
- [17] M. N. Achasov *et al.*, “Study of conversion decays $\phi \rightarrow \eta e^+ e^-$ and $\eta \rightarrow \gamma e^+ e^-$ in the experiment with SND detector at VEPP-2M collider.” *Phys. Lett. B* **504**, 275 (2001).
- [18] L. Adamczyk *et al.* (STAR Collaboration), “Measurements of D^0 and D^* production in $p + p$ collisions at $\sqrt{s} = 200$ GeV.” *Phys. Rev. D* **86**, 072013 (2012).
- [19] L. Adamczyk *et al.* (STAR Collaboration), “Observation of D^0 Meson Nuclear Modifications in $\text{Au} + \text{Au}$ Collisions at $\sqrt{s_{NN}} = 200\text{GeV}$.” *Phys. Rev. Lett.* **113**, 142301 (2014).
- [20] S. R. Klein *et al.*, *Comput. Phys. Commun.* **212**, 258 60 (2017).
- [21] F. Krauss, M. Greiner, and G. Soff, *Progress in Particle and Nuclear Physics* **39**, 503 (1997).

- 803 [22] R. C. Barrett and D. F. Jackson, *Nuclear Sizes and Structure (Oxford*
804 *University Press, 1977).*
- 805 [23] S. J. Brodsky, T. Kinoshita, and H. Terazawa, *Phys. Rev. D 4, 1532*
806 *(1971).*
- 807 [24] J. Adams *et al.* (STAR Collaboration), *Phys. Rev. C 70, 031902 (2004).*
- 808 [25] M. Dyndal *et al.* (ATLAS Collaboration), *Nuclear Physics A 967, 281*
809 *(2017).*
- 810 [26] E. Abbas *et al.* (ALICE Collaboration), *The European Physical Journal*
811 *C 73, 2617 (2013).*
- 812 [27] C. Loizides, J. Nagle, and P. Steinberg, *SoftwareX 1-2, 13 (2015).*